CrossMark

Testing the ΛCDM Cosmological Model with Forthcoming Measurements of the Cosmic Microwave Background with SPT-3G

K. Prabhu[1], S. Raghunathan[2], M. Millea[3], G. P. Lynch[1], P. A. R. Ade[4], E. Anderes[5], A. J. Anderson[6,7,8], B. Ansarinejad[9], M. Archipley[2,10], L. Balkenhol[11], K. Benabed[11], A. N. Bender[7,8,12], B. A. Benson[6,7,8], F. Bianchini[13,14,15], L. E. Bleem[7,12], F. R. Bouchet[11], L. Bryant[16], E. Camphuis[11], J. E. Carlstrom[7,8,12,16,17], T. W. Cecil[12], C. L. Chang[7,8,12], P. Chaubal[9], P. M. Chichura[7,17], A. Chokshi[18], T.-L. Chou[7,17], A. Coerver[3], T. M. Crawford[7,8], A. Cukierman[13,14,15], C. Daley[10], T. de Haan[19], K. R. Dibert[7,8], M. A. Dobbs[20,21], A. Doussot[11], D. Dutcher[22], W. Everett[23], C. Feng[24], K. R. Ferguson[25], K. Fichman[7,17], A. Foster[22], S. Galli[11], A. E. Gambrel[7], R. W. Gardner[16], F. Ge[1], N. Goeckner-Wald[13,14], R. Gualtieri[26], F. Guidi[11], S. Guns[3], N. W. Halverson[27,28], E. Hivon[11], G. P. Holder[24], W. L. Holzapfel[3], J. C. Hood[7], A. Hryciuk[7,17], N. Huang[3], F. Kéruzoré[12], L. Knox[1], M. Korman[29], K. Kornoelje[7,8], C.-L. Kuo[13,14,15], A. T. Lee[3,30], K. Levy[9], A. E. Lowitz[7], C. Lu[24], A. Maniyar[13,14,15], F. Menanteau[2,10], J. Montgomery[20], Y. Nakato[14], T. Natoli[7], G. I. Noble[31,32], V. Novosad[33], Y. Omori[7,8], S. Padin[7,34], Z. Pan[7,12,17], P. Paschos[16], K. A. Phadke[2,10], A. W. Pollak[18], W. Quan[7,17], M. Rahimi[9], A. Rahlin[6,7], C. L. Reichardt[9], M. Rouble[20], J. E. Ruhl[29], E. Schiappucci[9], G. Smecher[35], J. A. Sobrin[6,7], A. A. Stark[36], J. Stephen[16], A. Suzuki[30], C. Tandoi[10], K. L. Thompson[13,14,15], B. Thorne[1], C. Trendafilova[2], C. Tucker[4], C. Umilta[24], A. Vitrier[11], J. D. Vieira[2,10,24], Y. Wan[2,10], G. Wang[12], N. Whitehorn[37], W. L. K. Wu[13,15], V. Yefremenko[12], M. R. Young[6,7], and J. A. Zebrowski[6,7,8]

[1] Department of Physics & Astronomy, University of California, One Shields Avenue, Davis, CA 95616, USA; karthikprabhu22@gmail.com
[2] Center for AstroPhysical Surveys, National Center for Supercomputing Applications, Urbana, IL 61801, USA; srinirag@illinois.edu
[3] Department of Physics, University of California, Berkeley, CA 94720, USA
[4] School of Physics and Astronomy, Cardiff University, Cardiff CF24 3YB, UK
[5] Department of Statistics, University of California, One Shields Avenue, Davis, CA 95616, USA
[6] Fermi National Accelerator Laboratory, MS209, P.O. Box 500, Batavia, IL 60510, USA
[7] Kavli Institute for Cosmological Physics, University of Chicago, 5640 South Ellis Avenue, Chicago, IL 60637, USA
[8] Department of Astronomy and Astrophysics, University of Chicago, 5640 South Ellis Avenue, Chicago, IL 60637, USA
[9] School of Physics, University of Melbourne, Parkville, VIC 3010, Australia
[10] Department of Astronomy, University of Illinois Urbana-Champaign, 1002 West Green Street, Urbana, IL 61801, USA
[11] Sorbonne Université, CNRS, UMR 7095, Institut d'Astrophysique de Paris, 98 bis bd Arago, 75014 Paris, France
[12] High-Energy Physics Division, Argonne National Laboratory, 9700 South Cass Avenue, Lemont, IL 60439, USA
[13] Kavli Institute for Particle Astrophysics and Cosmology, Stanford University, 452 Lomita Mall, Stanford, CA 94305, USA
[14] Department of Physics, Stanford University, 382 Via Pueblo Mall, Stanford, CA 94305, USA
[15] SLAC National Accelerator Laboratory, 2575 Sand Hill Road, Menlo Park, CA 94025, USA
[16] Enrico Fermi Institute, University of Chicago, 5640 South Ellis Avenue, Chicago, IL 60637, USA
[17] Department of Physics, University of Chicago, 5640 South Ellis Avenue, Chicago, IL 60637, USA
[18] University of Chicago, 5640 South Ellis Avenue, Chicago, IL 60637, USA
[19] High Energy Accelerator Research Organization (KEK), Tsukuba, Ibaraki 305-0801, Japan
[20] Department of Physics and McGill Space Institute, McGill University, 3600 Rue University, Montreal, Quebec H3A 2T8, Canada
[21] Canadian Institute for Advanced Research, CIFAR Program in Gravity and the Extreme Universe, Toronto, ON M5G 1Z8, Canada
[22] Joseph Henry Laboratories of Physics, Jadwin Hall, Princeton University, Princeton, NJ 08544, USA
[23] Department of Astrophysical and Planetary Sciences, University of Colorado, Boulder, CO 80309, USA
[24] Department of Physics, University of Illinois Urbana-Champaign, 1110 West Green Street, Urbana, IL 61801, USA
[25] Department of Physics and Astronomy, University of California, Los Angeles, CA 90095, USA
[26] Department of Physics and Astronomy, Northwestern University, 633 Clark Street, Evanston, IL 60208, USA
[27] CASA, Department of Astrophysical and Planetary Sciences, University of Colorado, Boulder, CO 80309, USA
[28] Department of Physics, University of Colorado, Boulder, CO 80309, USA
[29] Department of Physics, Case Western Reserve University, Cleveland, OH 44106, USA
[30] Physics Division, Lawrence Berkeley National Laboratory, Berkeley, CA 94720, USA
[31] Dunlap Institute for Astronomy & Astrophysics, University of Toronto, 50 St. George Street, Toronto, ON M5S 3H4, Canada
[32] David A. Dunlap Department of Astronomy & Astrophysics, University of Toronto, 50 St. George Street, Toronto, ON M5S 3H4, Canada
[33] Materials Sciences Division, Argonne National Laboratory, 9700 South Cass Avenue, Lemont, IL 60439, USA
[34] California Institute of Technology, 1200 East California Boulevard, Pasadena, CA 91125, USA
[35] Three-Speed Logic, Inc., Victoria, B.C., V8S 3Z5, Canada
[36] Harvard-Smithsonian Center for Astrophysics, 60 Garden Street, Cambridge, MA 02138, USA
[37] Department of Physics and Astronomy, Michigan State University, East Lansing, MI 48824, USA

Abstract

We forecast constraints on cosmological parameters enabled by three surveys conducted with SPT-3G, the third-generation camera on the South Pole Telescope. The surveys cover separate regions of 1500, 2650, and 6000 deg^2 to different depths, in total observing 25% of the sky. These regions will be measured to white noise levels of

roughly 2.5, 9, and 12 μK-arcmin, respectively, in cosmic microwave background (CMB) temperature units at 150 GHz by the end of 2024. The survey also includes measurements at 95 and 220 GHz, which have noise levels a factor of $\sim$1.2 and 3.5 times higher than 150 GHz, respectively, with each band having a polarization noise level $\sim\sqrt{2}$ times higher than the temperature noise. We use a novel approach to obtain the covariance matrices for jointly and optimally estimated gravitational lensing potential band powers and unlensed CMB temperature and polarization band powers. We demonstrate the ability to test the ΛCDM model via the consistency of cosmological parameters constrained independently from SPT-3G and Planck data, and consider the improvement in constraints on ΛCDM extension parameters from a joint analysis of SPT-3G and Planck data. The ΛCDM cosmological parameters are typically constrained with uncertainties up to $\sim$2 times smaller with SPT-3G data, compared to Planck, with the two data sets measuring significantly different angular scales and polarization levels, providing additional tests of the standard cosmological model.

Unified Astronomy Thesaurus concepts: Cosmic microwave background radiation (322); Cosmological parameters (339)

1. Introduction

Observations of the cosmic microwave background (CMB) temperature and polarization anisotropies have played a crucial role in the field of cosmology, particularly in the establishment of a six-parameter standard cosmological model, ΛCDM. This model, which provides an excellent fit to CMB data from Planck (Planck Collaboration et al. 2020), the Atacama Cosmology Telescope (ACT; Aiola et al. 2020; Choi et al. 2020; Madhavacheril et al. 2024), the South Pole Telescope (SPT; Simard et al. 2018; Dutcher et al. 2021; Balkenhol et al. 2021; Pan et al. 2023), as well as a great variety of other astrophysical data sets (Alam et al. 2021; DES Collaboration 2024; Abbott et al. 2022; Kuijken et al. 2019), has been enormously successful in providing a consistent framework for understanding the universe.

These successes are perhaps surprising since critical ingredients to the model (dark matter, dark energy, and the generator of primordial fluctuations) appear disconnected from the physics we know of through laboratory experiments. The desire for clues that could deepen our understanding of these ingredients motivates us to continue our testing of the model. One particularly compelling line of testing emerges from the fact that the standard cosmological model, conditioned on data from the Planck satellite, makes extremely precise predictions for the CMB temperature, polarization, and lensing power spectra on angular scales not well measured by Planck.

Additional motivation for testing ΛCDM (beyond our ignorance about dark matter, dark energy, and the generator of primordial fluctuations) comes from cosmological tensions and anomalies as these might be evidence for beyond-ΛCDM physics. A prominent issue is the Hubble tension, a notable discrepancy between classical distance ladder determinations (Murakami et al. 2023; Riess et al. 2022) and ΛCDM-dependent determinations (Planck Collaboration et al. 2020) of the current expansion rate of the universe. An additional, though statistically weaker tension, is in the values of σ_8, the rms of the density field smoothed over $8h^{-1}$ Mpc radius spheres, derived from weak lensing observations in optical galaxy surveys and those inferred from CMB data[38] (Asgari et al. 2021; Joudaki et al. 2020; Abbott et al. 2022). There are also peculiar patterns in the CMB temperature anisotropies on large angular scales, which, by some calculations, are extremely unlikely in a ΛCDM universe (Copi et al. 2010; Givans & Kamionkowski 2023).

Altogether these discrepancies offer some evidence that ΛCDM is not the final word in cosmology, encouraging us to search for beyond-ΛCDM signals in our surveys. Indeed, there are alternative models that reduce the σ_8 or H_0 tensions and make different predictions for the power spectra than is the case for ΛCDM. In this context, it becomes pertinent to investigate the extent to which upcoming observational data can distinguish between the standard ΛCDM model and some of these alternatives.

SPT-3G, the third-generation camera on the SPT, has the potential to test the ΛCDM model by precisely mapping the primary and lensing anisotropies of the CMB. The full SPT-3G data set will comprise three surveys, which, altogether, cover 10,000 deg^2, or $\sim$25% of the sky. The SPT-3G Main survey (1500 deg^2), observed over five austral winters, is approaching the target depths of the next-generation CMB-S4 Deep and Wide survey of 70% of the sky planned to begin in the next decade (Abazajian et al. 2022). Next-deepest is the SPT-3G Summer survey, a completed collection of three fields observed during four austral summers totaling 2650 deg^2. The shallowest is the 6000 deg^2 SPT-3G Wide survey, which, after one observing season, will still be deeper than surveys from any other existing high-resolution CMB experiment of comparable survey size.

Besides mapping the primary CMB and lensing anisotropies, SPT-3G will provide a powerful set of data for studying a broad range of topics in cosmology and astrophysics. These include the delensing of lensing-induced B-modes (Ade et al. 2021); production of mass-limited catalogs of galaxy clusters out to high redshifts using the thermal Sunyaev–Zel'dovich (tSZ) signature (Bleem et al. 2015; Huang et al. 2020; Bleem et al. 2020, 2024), and constraining cosmology with these catalogs (Bocquet et al. 2024); robust measurements of the kinematic Sunyaev–Zel'dovich (kSZ) signal for velocity reconstruction and constraining the epoch of reionization (Schiappucci et al. 2023; Raghunathan & Omori 2023; Raghunathan et al. 2024); production of millimeter-wave point-source catalogs (Everett et al. 2020); and the detection and monitoring of millimeter-wave galactic, extragalactic, and solar system transient, variable, and moving objects (Whitehorn et al. 2016; Guns et al. 2021; Chichura et al. 2022; Hood et al. 2023; Tandoi et al. 2024).

Here, we demonstrate the capacity of the SPT-3G surveys to test ΛCDM in several ways, focusing exclusively on the constraining power of CMB and lensing power spectrum measurements. We forecast how well we will measure the temperature and *E*-mode polarization power spectra, their cross

---

[38] Although this tension is partially resolved in the analysis of Planck PR4 maps (Tristram et al. 2024).

power spectrum, and the power spectrum of the lensing potential.

We also propagate the power spectrum uncertainties forward to constraints on cosmological parameters. From SPT-3G data alone we can obtain constraints on the parameters of the ΛCDM model that are comparable to, and in some cases, better than those from Planck. When compared to Planck, a greater fraction of the weight of these constraints comes from polarization (see Galli et al. 2014, for example), from smaller angular scales, and from lensing. Therefore, comparison of these parameter estimates with those from Planck will be an excellent test of the ΛCDM model.

The outcome of such a test could provide evidence for physics beyond ΛCDM. Looking ahead to this scenario, we also forecast constraints on single- and double-parameter extensions of ΛCDM from the combination of Planck and SPT-3G data and report how these constraints improve upon those from Planck alone. The test could equally well reveal consistency with ΛCDM, an outcome that should not be dismissed given the model's track record. If this is the case, joint Planck+SPT-3G ΛCDM parameter constraints will be of interest, and we provide forecasts for the combined constraints on ΛCDM as well.

In addition to our comparison with Planck, we compare with forecasts we make for the high-resolution survey of the Simons Observatory (SO; Simons Observatory Collaboration 2019). SO is expected to survey roughly 40% of the sky (much more sky is available to survey from midlatitude sites such as the SO site in the Atacama Plateau in Chile compared to the South Pole) to noise levels similar to or slightly better than the SPT-3G Summer fields, leading to constraints on ΛCDM parameters that are comparable to what we expect from the combined SPT-3G surveys.

For an ongoing analysis of the first two full years of data from the SPT-3G Main survey, one of our analysis approaches is a Bayesian one, which is in principle unbiased and optimal (information lossless) despite the presence of gravitational lensing, and naturally results in joint constraints on the lensing power spectrum and unlensed CMB power spectra. To speed up the estimation of the unlensed and lensing power spectra, from this likelihood, we employ the Marginal Unbiased Score Expansion (MUSE) technique (Millea & Seljak 2022). We refer to this whole inference pipeline from maps to the band powers and their covariance matrix as MUSE. Since MUSE can be used to obtain a covariance matrix for all the relevant spectra, it is quite convenient for us to propagate these uncertainties to a parameter error covariance matrix, and compare the results with more traditional forecasting techniques.

This paper is structured as follows: In Section 2, we describe the specifications of the SPT-3G instrument, the survey regions, and our assumptions about the noise and foregrounds. In Section 3, we describe the methodology used to obtain these forecasts. We report the forecasts of the parameter constraints for ΛCDM with SPT-3G alone and for extensions with SPT-3G combined with Planck in Section 4. In Section 5, we discuss prospects for SPT-3G to detect departures from ΛCDM predictions and test alternate models. Finally, we summarize our findings in Section 6.

In this work, we set the fiducial values of the baseline ΛCDM cosmology and its extensions to Planck 2018 measurements (TT, TE, EE + lowE + lensing in Table 2 of Planck Collaboration et al. 2020) and compute the theoretical CMB power spectra using CAMB software (Lewis et al. 2000).

2. Experiment Specifications

In this section, we briefly describe the specifications of the SPT-3G experiment along with the details of the three survey regions and a description of the noise characteristics.

2.1. Survey Specifications

SPT is a 10 m diameter telescope specifically engineered for low-noise and high-resolution measurements of the millimeter-wave sky. The telescope is currently equipped with SPT-3G, the third CMB camera installed on SPT. SPT-3G is a significant upgrade compared to previous cameras, incorporating a polarization-sensitive tri-chroic focal plane with almost 16,000 detectors, operating in three frequency bands, 95, 150, and 220 GHz. For more details about the instrument, we refer the readers to Benson et al. (2014), Bender et al. (2018), Anderson et al. (2018), and Sobrin et al. (2018, 2022).

One of the primary science goals of SPT-3G is to create a template of the gravitational-lensing-induced B-modes in the patch of sky observed by the BICEP-Keck (BK) family of experiments. This template can be subtracted from the BK data, reducing the primary source of variance in the BK B-mode analysis and potentially improving the sensitivity to primordial gravitational waves by a factor of 3. To that end, since 2019, SPT-3G has been used primarily (8 months per yr) to observe the 1500 deg^2 SPT-3G Main survey, which overlaps completely with the BICEP3 and BICEP Array sky coverage (see Figure 1). During the austral summer season (roughly at the beginning of December), when the Sun is above the horizon and gets sufficiently close to the SPT-3G Main survey region, it is picked up by the telescope far sidelobes. Therefore, until sunset, we switch to observing three fields that are safe from Sun contamination. These comprise the 2650 deg^2 SPT-3G Summer survey (Figure 1). We refer to these three fields as Summer-A, Summer-B, and Summer-C.

Even with the added sky coverage of the Summer survey, the constraints on ΛCDM parameters from SPT-3G data are limited by sample variance. For this reason, we have paused our standard observing strategy for 1 yr to undertake a new survey of all the sky viewable from the South Pole at instrumentally feasible observing elevations and with minimal Galactic foreground contamination. We have empirically determined that, during the winter, we are able to observe with SPT-3G between elevations of roughly 20° and 80° (limited by detector linearity at the low end and refrigerator performance on the high end). The intersection of these elevation limits (which, at the South Pole, correspond directly to declination limits) and the Planck GAL080 (Planck Collaboration et al. 2016b) Galactic mask defines our new SPT-3G Wide survey, which totals 6000 deg^2 and is shown in Figure 1. Observations of the SPT-3G Wide survey commenced in December of 2023 and will continue through the austral winter of 2024. We will refer to the combination of the SPT-3G Main and the SPT-3G Summer surveys as the Ext-4k survey. Similarly, we will refer to the combination of SPT-3G Main, SPT-3G Summer, and SPT-3G Wide surveys as the Ext-10k survey. In Table 1, we summarize the areas and depths for the SPT-3G Main, Summer, and Wide surveys.
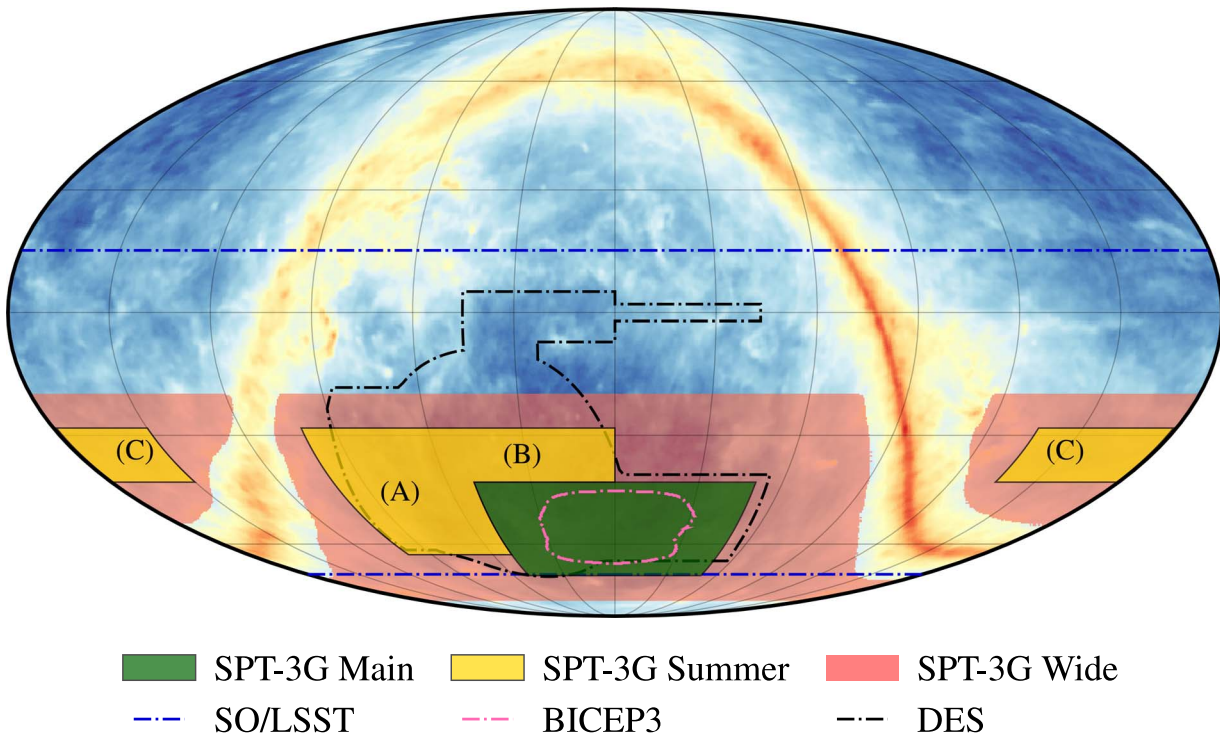
Figure 1. Footprints of the three SPT-3G surveys: SPT-3G Main (green), SPT-3G Summer (yellow), and SPT-3G Wide (red). Also shown are the footprints of other surveys: BICEP3 (pink dashed–dotted), DES (black dashed–dotted), and SO/LSST (blue dashed–dotted). The background is the map of the galactic dust produced by the Planck satellite (Planck Collaboration et al. 2016a).

The survey footprints for SPT-3G and other surveys are shown in Figure 1. As is evident from the figure, all three SPT-3G surveys have an excellent overlap with SO, which will enable a variety of cross checks to be performed between the two surveys. We list the noise levels and the field centers for the SPT-3G surveys in Table 1. In this work, we produce forecasts both for current noise levels (2019–2023) and for the ones expected from future SPT-3G observations (2024–2026). In addition to instrumental noise, our data is also affected by atmospheric noise, which increases toward large angular scales. We model the temperature noise power spectrum as

$$N_\ell = \Delta_T^2 \left[1 + \left(\frac{\ell}{\ell_{\mathrm{knee},T}} \right)^{\alpha_T} \right], \qquad (1)$$

where Δ_T represents the white noise level at a given band in μK-arcmin, $\ell_{\mathrm{knee},T}$, and α_T are used to parameterize the atmospheric noise. For the SPT-3G Main survey, we adopt the values of ℓ_{knee} and α in Table 2 from previous analyses, but we find that the results of our forecasting are insensitive to the exact values of ℓ_{knee} and α. For the SPT-3G Summer survey, during which the atmospheric opacity and precipitable water vapor levels are higher, we fit real noise data to the model in Equation (1), and the parameters in Table 2 are the result of those fits. We also adopt the SPT-3G Summer survey parameters for the SPT-3G Wide survey (which is likely pessimistic for the higher-elevation Wide fields). We extrapolate the white noise levels for deeper integration times. We also fit the noise model parameters for the polarization maps in a similar way. We note that the white noise levels in the polarization maps are roughly $\sqrt{2} \times$ higher than in the temperature maps. In Table 2, we list the ℓ_{knee} and α values

adopted for different bands for both temperature and polarization. Finally, we deconvolve the experimental beam window function B_ℓ from the noise spectra as $N'_\ell \equiv \frac{N_\ell}{B_\ell^2}$, where the beam window function at each frequency is estimated as detailed in Dutcher et al. (2021). We show the model noise spectra in different bands (90 GHz in green, 150 GHz in yellow, and 220 GHz in red) for all the SPT-3G surveys in Figure 2. These spectra assume integration times of 5 yr for the SPT-3G Main survey, 4 yr for the SPT-3G Summer survey, and 1 yr for the SPT-3G Wide survey.

3. Forecasting Methodology

In this section, we outline the two methods used for calculating the band power covariance matrix from which a Fisher matrix for cosmological parameters (Tegmark et al. 1997) can be derived. The first method relies on an analytic approximation (see Section 3.2) for the covariance matrix. This approach has been widely adopted in various forecasting studies, and is quite simple and flexible. Our second method employs MUSE (see Section 3.3), which is one of the analysis pipelines developed for SPT-3G data. MUSE is more accurate as it readily incorporates nonideal factors such as covariance between multipoles, covariance between different types of power spectra, and impacts of delensing. Although previous works (for example, Hotinli et al. 2022; Trendafilova 2023), suggest that these factors may not significantly alter our forecasts, adopting both these methods improves the robustness and reliability of our forecasts. We also describe the method we use to combine Planck data with SPT-3G. We begin with a brief description of how we optimally combine data from multiple frequency bands.

Table 1
Sky Fraction and Temperature White Noise Levels in the Three Bands for the Different SPT Surveys Considered in This Work

Survey	Area (deg^2)	R.A. Center (deg)	Decl. Center (deg)	Years Observed	Noise Level (Δ_T) [μK-arcmin]			
					95 GHz	150 GHz	220 GHz	Coadded
Completed:								
SPT-3G Main	1500	0	−57.5	2019–2023	3.0	2.5	8.9	1.9
SPT-3G Summer-A	1210	75.0	−42.0		9.4	8.7	29.5	6.2
SPT-3G Summer-B	570	25	−36		10.0	9.7	30.3	6.8
SPT-3G Summer-C	860	187.5	−38		10.0	9.2	27.8	6.6
Ongoing+Future:								
SPT-3G Main	1500	0	−57.5	2019–2023 + 2025–2026	2.5	2.1	7.6	1.6
SPT-3G Wide	6000	Multiple		2024	14	12	42	8.8

Note. The polarization white noise levels are expected to be $\sim\sqrt{2}$ times higher

Table 2
Atmospheric Noise Specifications for the Three SPT Bands

Specification	Observation Band		
	90 GHz	150 GHz	220 GHz
SPT-3G Main:			
$\ell_{\mathrm{knee},T}$	1200	2200	2300
α_T	−3	−4	−4
$\ell_{\mathrm{knee},P}$		300	
α_P		−1	
SPT-3G Summer and SPT-3G Wide:			
$\ell_{\mathrm{knee},T}$	1600	2600	2600
α_T	−4.5	−4	−3.9
$\ell_{\mathrm{knee},P}$	300	490	500
α_P	−2.2	−2	−2.5

3.1. Linear Combination of Frequency Bands

We combine data from multiple frequency bands listed in Table 1 using a scale-dependent linear combination (LC) technique (Cardoso et al. 2008; Planck Collaboration et al. 2014). In harmonic space denoted by subscript ℓ, this corresponds to

$$S_{\ell m} = \sum_{i=1}^{N_{\mathrm{bands}}} w_\ell^i M_{\ell m}^i, \qquad (2)$$

where S is the desired sky signal (in our case the CMB), w_ℓ is the weight, $M_{\ell m}$ is the spherical harmonic transform of the input map, and the subscript i runs over all the frequency bands. The multipole-dependent weights w_ℓ are tuned in order to minimize the overall variance from noise and foregrounds. They are derived as

$$w_\ell = \frac{C_\ell^{-1} A_s}{A_s^\dagger C_\ell^{-1} A_s}. \qquad (3)$$

Here, C_ℓ is a $N_{\mathrm{bands}} \times N_{\mathrm{bands}}$ matrix containing the covariance of noise and foregrounds across different frequencies at a given multipole ℓ; $A_s = [1\ 1..1]$ is the frequency response of the CMB in different bands and is a $N_{\mathrm{bands}} \times 1$ vector.

The noise modeling is described in Section 2.1.

The foreground signal receives contributions from both the galactic and extragalactic signals. In our baseline approach, we ignore the galactic foreground signals by introducing sky cuts but we perform tests to assess their impact using pySM simulations in Section 4.1.2. The extragalactic foreground can be decomposed into signals from radio galaxies, dusty star-forming galaxies (DSFG), tSZ, and kSZ signals. We model these using measurements from Reichardt et al. (2021). To this end, we assume a conservative point-source masking threshold, similar to that of Reichardt et al. (2021), and remove sources with flux above $S_{150} = 6$ mJy. For the radio galaxies, we assume a spectral index of $\alpha_{\mathrm{radio}} = -0.76$ (Reichardt et al. 2021) to model their frequency dependence. On the other hand, the DSFG contribution is split into clustering and Poisson components, which are both modeled using a modified blackbody model with $T_{\mathrm{CIB}} = 25$K, and $\beta_{\mathrm{CIB-Clus}} = 2.2$ and $\beta_{\mathrm{CIB-Poi}} = 1.5$ for the clustering and Poisson terms, respectively. For the polarization power spectrum EE, we scale the above TT power spectrum of sources as $C_\ell^{EE} = P^2 C_\ell^{TT}$ assuming a polarization fraction of $P = 3\%$ ($P = 2\%$) for radio galaxies (DSFG) based on Datta et al. (2019) and Gupta et al. (2019). We also remove the contribution from clusters detected at a signal-to-noise ratio (S/N) $\geqslant 5$, which roughly corresponds to $M_{500c} \gtrsim 10^{14} M_\odot$ (see Figure 5 of Raghunathan 2022). For kSZ, we assume a flat $D_\ell = 3\ \mu$K^2 for all the bands. The tSZ and kSZ signals are assumed to be unpolarized, and hence we ignore the contribution from clusters on C_ℓ^{EE} and C_ℓ^{TE}.

We also note here that the instrumental bandpass of the individual frequency bands are not delta functions and are roughly 25, 30, and 50 GHz for 95, 150, and 220 GHz bands, respectively (Sobrin et al. 2022). The frequency responses of the detectors are calculated using a Fourier transform spectrometer. With these bandpass measurements, we calculate the effective frequencies ν_{eff} for each of the foreground signals described above to compute their respective power spectra. For simplicity, we assume the values of ν_{eff} to be the same as the ones reported in Reichardt et al. (2021) although the bandpasses of the current SPT-3G receiver are slightly different (see Figure 7 of Sobrin et al. 2022). We checked the impact of the difference in the bandpasses, and it has a negligible impact
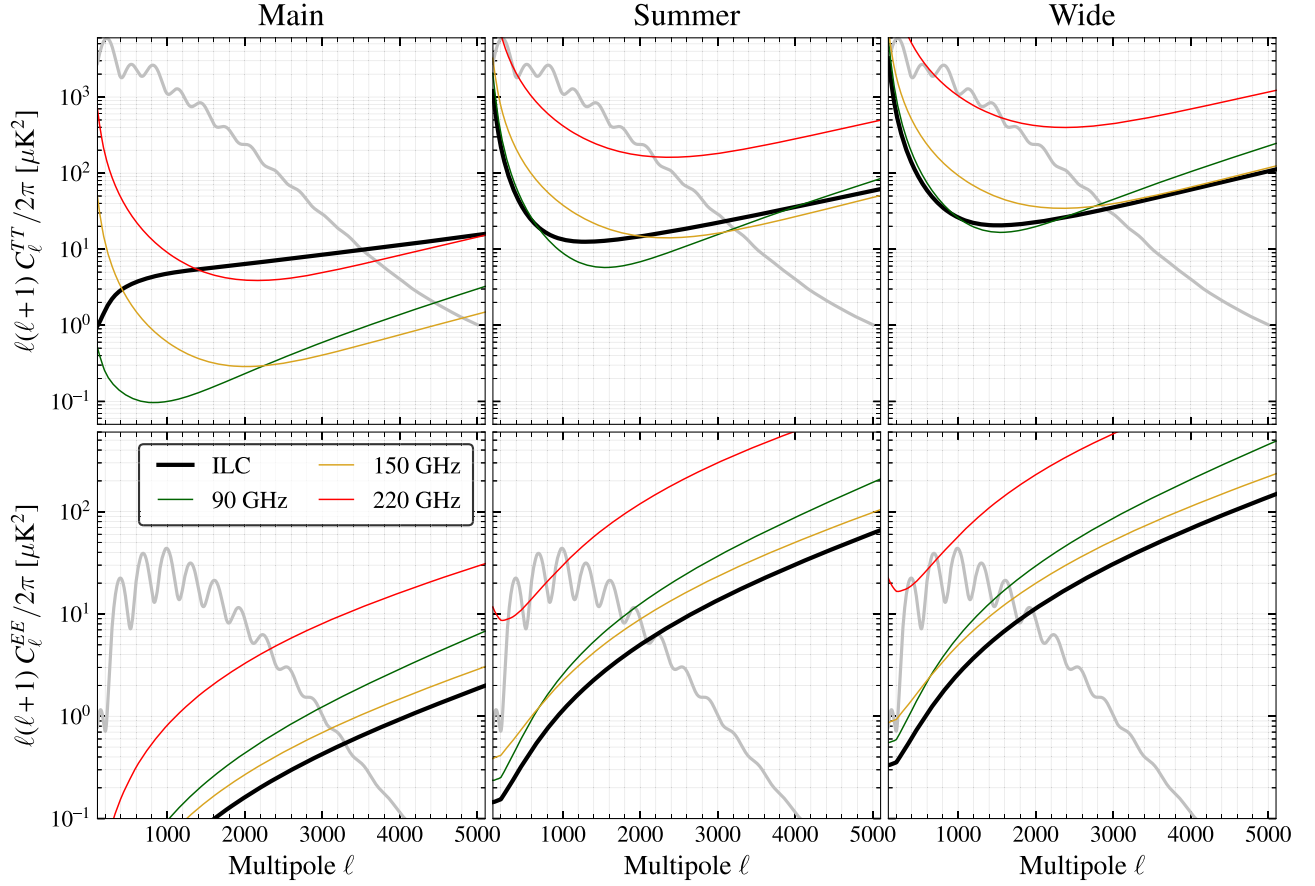
Figure 2. Expected *TT* and *EE* noise power spectra for the three SPT-3G surveys: beam-deconvolved noise curves in the three bands for SPT-3G Main (5 yr), Summer (4 yr), and Wide (1 yr) surveys are shown as colored curves. The MV combination of the LC residuals is the thick black solid curve in all the panels. The gray curves represent the CMB power spectra. Top panels are for temperature and the bottom panels are for polarization. The LC residuals are dominated by foregrounds for temperature for SPT-3G Main while for polarization they are roughly equal to the inverse variance weighted noise spectra from the three bands.

on the foreground modeling and the constraints reported in this work.

In Figure 2, we show the LC residuals for all three SPT-3G surveys as the thick black solid curve. The top and bottom panels of the figure are for CMB temperature (*TT*) and polarization (*EE*) power spectra, denoted as gray curves. In the absence of foregrounds, the LC residuals simply correspond to the inverse variance combination of noise from different frequency bands, which is almost true for *EE* (bottom panels).

In Figure 3, we present the S/N per multipole for *TT/EE/TE/ϕϕ* spectra for SPT-3G Main (green) and Ext-10k (orange) surveys along with Planck (black). The power spectrum errors were calculated using the analytical formula (see Equation (5); Knox 1995; Jungman et al. 1996; Zaldarriaga et al. 1997). Planck has a higher S/N on large scales because of the larger sky coverage. However, the S/Ns of the SPT-3G Main and Ext-10k surveys are much higher than Planck on small scales. In particular, the S/Ns for the Ext-10k survey will surpass Planck beyond $\ell = 1800$, 800, and 450 for *TT*, *TE*, and *EE*, respectively. For *ϕϕ*, the S/N is better than Planck on all scales. As a result, we can expect significant improvement in cosmological parameters that control structure formation and that are sensitive to the damping tail from SPT-3G compared to Planck as we show later in this work.

3.2. Analytic Method

Given a set of power spectra of the lensed CMB and the lensing potential, $X, Y \in [TT, EE, TE, \phi\phi]$, the Fisher matrix is given by

$$\mathcal{F}_{ij} = \sum_{X,Y} \sum_{\ell} \frac{\partial C_\ell^X}{\partial \theta_i} \cdot (\Sigma_\ell^{-1})_{XY} \cdot \frac{\partial C_\ell^Y}{\partial \theta_j}, \quad (4)$$

where θs correspond to the cosmological parameters being constrained. The partial derivatives of the spectra with respect to the parameters θ, denoted as $\partial C_\ell / \partial \theta_j$, are obtained using the finite difference method. Σ_ℓ is the covariance of the power spectra, given by Equation (5)

$$\Sigma_\ell = \frac{2}{(2\ell+1)f_{\text{sky}}} \begin{pmatrix} (\tilde{C}_\ell^{TT})^2 & (C_\ell^{TE})^2 & \tilde{C}_\ell^{TT} C_\ell^{TE} & (C_\ell^{T\phi})^2 \\ (C_\ell^{TE})^2 & (\tilde{C}_\ell^{EE})^2 & \tilde{C}_\ell^{EE} C_\ell^{TE} & (C_\ell^{E\phi})^2 \\ \tilde{C}_\ell^{TT} C_\ell^{TE} & \tilde{C}_\ell^{EE} C_\ell^{TE} & \frac{1}{2}[(C_\ell^{TE})^2 + \tilde{C}_\ell^{TT} \tilde{C}_\ell^{EE}] & C_\ell^{T\phi} C_\ell^{E\phi} \\ (C_\ell^{T\phi})^2 & (C_\ell^{E\phi})^2 & C_\ell^{T\phi} C_\ell^{E\phi} & (\tilde{C}_\ell^{\phi\phi})^2 \end{pmatrix}, \quad (5)$$

where f_{sky} is the fraction of the sky for the survey under consideration and

$$\tilde{C}_\ell^X = C_\ell^X + N_\ell^X, \quad (6)$$
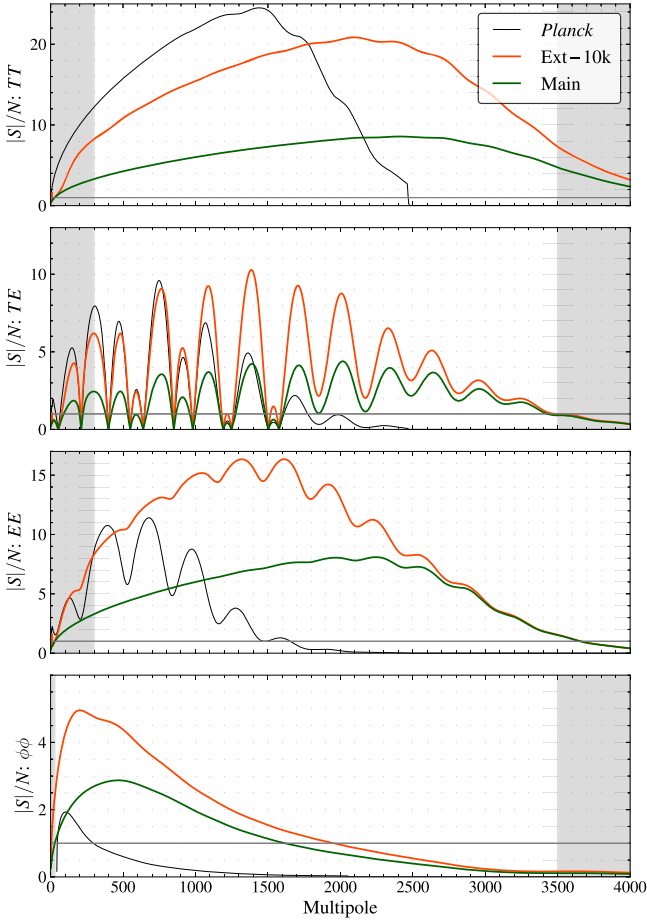
Figure 3. S/N per multipole on the primary and lensing CMB power spectra for the SPT-3G Main (green) and the Ext-10k (orange) SPT-3G surveys, with values for Planck (black) plotted for comparison. The constraining power of the full Ext-10k survey will be larger than Planck at $\ell \gtrsim 1800$ in TT, $\ell \gtrsim 800$ in TE, $\ell \gtrsim 450$ in EE, and effectively for all the modes in $\phi\phi$. The non-shaded area corresponds to the range of multipoles used in the forecasts.

Table 3
Fiducial Values of the Parameters and Priors Used in This Work

Parameter	Fiducial	Prior
ΛCDM parameters:		
Amplitude of scalar fluctuations $\ln(10^{10}A_s)$	3.044	...
Dark matter density $\Omega_c h^2$	0.1200	...
Baryon density $\Omega_b h^2$	0.02237	...
Scalar spectral index n_s	0.9649	...
Hubble parameter h	0.6732	...
Reionization optical depth τ_{re}	0.0544	0.007
Extensions:		
Sum of neutrino masses $\sum m_\nu$	0.06 eV	...
Number of relativistic species N_{eff}	3.044	...
Running of the spectral index n_{run}	0	...
Spatial curvature Ω_k	0	...
Equation of state of dark energy w_0	−1	...
Helium abundance Y_P[a]	0.245	...

Notes. All the applied priors are Gaussian with the widths given below in the table.
[a] Set from Big Bang nucleosynthesis consistency when Y_P is not included in the extension.

$X = \{TT, EE, \phi\phi\}$. N_ℓ^{TT} and N_ℓ^{EE} are the residual noise and foreground power after combining data from all the bands using the LC method. $N_\ell^{\phi\phi}$ is the lensing reconstruction noise derived using a quadratic lensing estimator (Hu & Okamoto 2002). In Table 3, we list the fiducial values of the cosmological parameters at which the Fisher matrix is evaluated and associated priors.

We calculate the Fisher matrix for each of the SPT-3G surveys given in Table 1 and combine them to obtain the final SPT-3G Fisher matrices as

$$\mathcal{F}_{Summer} = \mathcal{F}_{Summer-A} + \mathcal{F}_{Summer-B} + \mathcal{F}_{Summer-C}$$
$$\mathcal{F}_{Ext-4k} = \mathcal{F}_{Main} + \mathcal{F}_{Summer}$$
$$\mathcal{F}_{Ext-10k} = \mathcal{F}_{Main} + \mathcal{F}_{Summer} + \mathcal{F}_{Wide}. \quad (7)$$

The parameter covariance matrices are then obtained by inverting the Fisher matrix. We fix the ℓ ranges for all the SPT-3G surveys to the following for the Fisher matrix calculation: $300 \leqslant \ell \leqslant 3500$ for TT/TE; $300 \leqslant \ell \leqslant 4000$ for EE; and $30 \leqslant L \leqslant 3500$ for $\phi\phi$. For lensing reconstruction, we use $300 \leqslant \ell \leqslant 3500$ for T and $300 \leqslant \ell \leqslant 4000$ for P. We ignore $\ell > 3500$ in TT/TE because of the difficulties in modeling the extragalactic foreground signals in the temperature data. We have checked the correlations between the SPT-3G Main and the contiguous SPT-3G Summer surveys and we have found that they are negligible. This is due to the fact that we do not include the large-scale modes $\ell \leqslant 300$. Since the extragalactic foregrounds are largely unpolarized (Datta et al. 2019; Gupta et al. 2019), we can set a higher ℓ_{max} for EE. We find that extending $\ell_{max}^{EE} > 4000$ results in marginal improvements, indicating those modes are noise dominated, as can be inferred from Figure 3.

3.3. MUSE

MUSE (Millea & Seljak 2022) is a general algorithm for approximate marginalization over arbitrary latent parameters, which yields Gaussianized, asymptotically unbiased, and near-optimal constraints on parameters of interest. In our application of MUSE, the parameters of interest are the unlensed TT, TE, EE, and $\phi\phi$ band powers, which are weighted averages of the respective power spectra across defined multipole bins. These band powers depend on the latent parameters, which are the pixel values of the lensing map and the unlensed CMB field maps.

As previously demonstrated by Millea et al. (2021) using SPTpol data, the standard quadratic lensing estimator is suboptimal for lensing reconstruction at noise levels below $\Delta_T \sim 5\mu K - \text{arcmin}$ (Hirata & Seljak 2003a, 2003b) and hence, using MUSE has an advantage in terms of the lensing reconstruction. Another advantage of MUSE is that it performs optimal delensing on the lensed CMB maps and produces estimates of the unlensed power spectra, lensing potential power spectra and their joint covariance. This covariance naturally includes lensing-induced correlations between different band powers ($\ell - \ell'$), and also between delensed CMB $TT/EE/TE$ and lensing $\phi\phi$ spectra (Peloton et al. 2017; Trendafilova 2023).

Despite the above advantages, we do not expect a significant improvement in the constraints from using MUSE over quadratic estimator (QE) methods. This is because the lensing
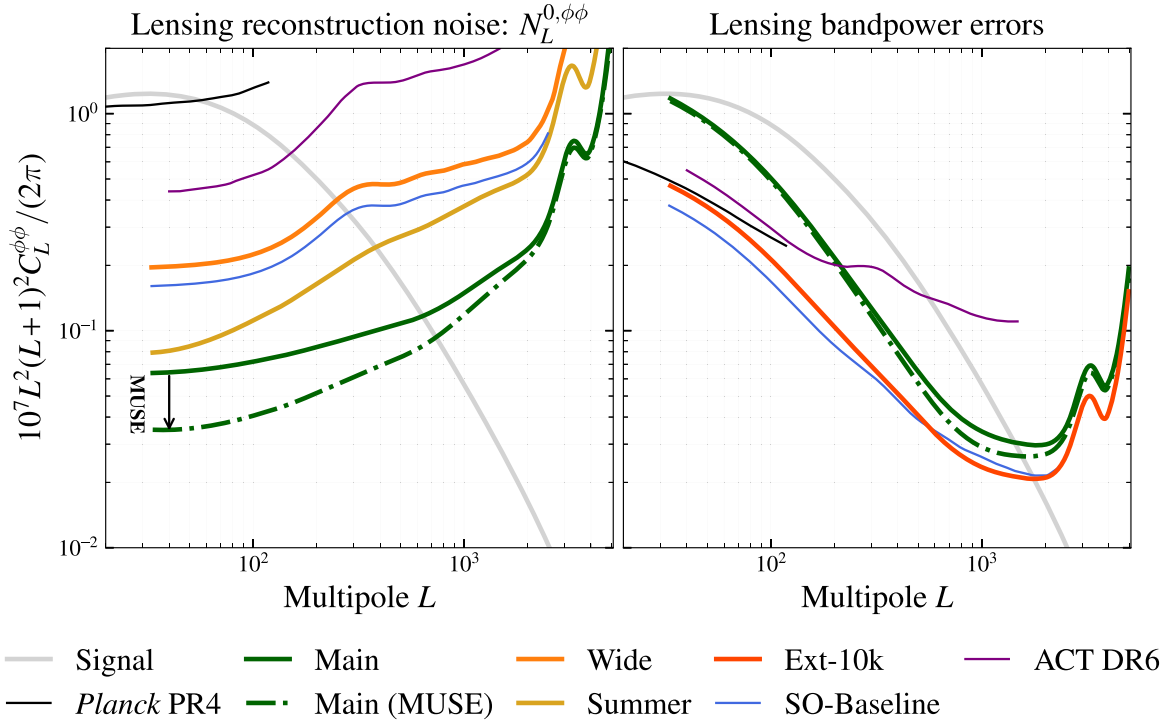
Figure 4. Left panel: lensing reconstruction noise $N_L^{(0,\phi\phi)}$ power spectra for the SPT-3G surveys along with Planck, SO, and ACT. For the SPT-3G Main survey, we show two curves: solid green for QE and dashed–dotted green for MUSE. For SPT-3G Main survey noise levels, lensing noise from MUSE is roughly $\times 2$ better than QE at large scales. For other surveys, the difference between MUSE and QE is negligible and hence, not shown. Right panel: band power errors for the lensing power spectrum (gray) from different surveys. While the lensing reconstruction noise $N_L^{(0,\phi\phi)}$ is lower on large scales for MUSE, the band power errors are not significantly different as they are dominated by the sample variance.

band power errors are dominated by sample variance over the angular scales for which MUSE reduces ϕ map noise, and the lensing-induced correlations are not important for the current noise levels. Moreover, the optimality of MUSE is non-negligibly better only for the SPT-3G Main survey, and not for the others given their higher noise levels (see Table 1).

The optimality of the MUSE estimates is useful for other purposes like delensing the lensing-induced B-modes and cross correlations, at least for the SPT-3G Main survey with its low-noise levels (see Table 1). We demonstrate this in Figure 4, which shows the lensing reconstruction noise $N_L^{(0,\phi\phi)}$ for different surveys. For the SPT-3G Main survey shown in green, the lensing reconstruction noise goes down by roughly $\times 2.5$ ($\times 1.9$) for polarization-only (including temperature information) lensing estimators when we replace QE (solid) with MUSE (dashed–dotted). As mentioned above, the difference between QE and MUSE is negligible for other surveys, and hence, not shown.

In MUSE, we express the lensing and unlensed CMB power spectra as scaled versions of the fiducial power spectra, which, for our purposes, are based on the Planck 2018 spectra (Planck Collaboration et al. 2020). This is given by

$$C_\ell = A_\ell C_\ell^{\rm fid}, \tag{8}$$

where $C_\ell^{\rm fid}$ represents the fiducial power spectrum, and A_ℓ is the scaling factor applied to this fiducial spectrum. Here, C_ℓ is used as a general notation that encompasses all types of power spectra, including unlensed $TT/TE/EE$ and $\phi\phi$.

In our application of MUSE, we do not estimate the power at each individual multipole but instead band power parameters, A_b, that each scale a fiducial power spectrum across a band of

width $\Delta\ell = 100$. As a result, MUSE produces a covariance matrix of these scaling coefficients $\Sigma_{A_b} \equiv \langle A_b A_b^* \rangle$. The A_b can be understood as the binned version of A_ℓ.

As described below, this covariance is subsequently utilized to construct the cosmological parameter-Fisher matrix, from which we derive the constraints on parameters. We provide more details about MUSE in the appendices. Specifically, we describe the derivation of the MUSE covariance matrix in Appendix A, the simulations used for estimating the covariance matrix in Appendix A.1, and the lensing reconstruction noise in Appendix A.2.

The standard Fisher formula described in the previous section Equation (4) can be adapted to incorporate the MUSE covariance matrix Σ_{A_b}. Let the covariance matrix of the power spectra be represented by Σ_{C_ℓ} and the covariance matrix of the amplitudes be represented by Σ_{A_ℓ}, then the Fisher matrix can be written as
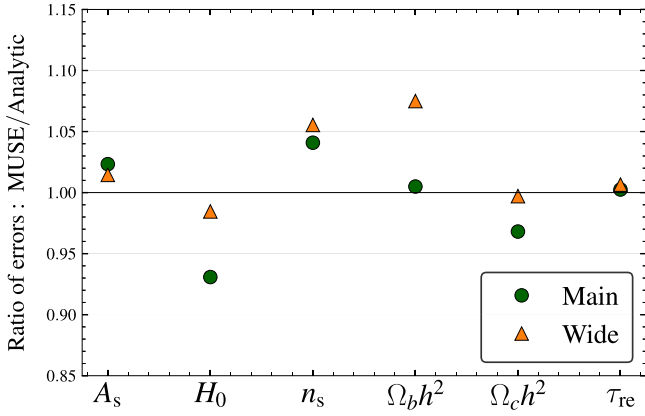
$$\mathcal{F}_{ij} = \sum_{XY}\sum_{\ell\ell'} \frac{\partial C_\ell^X}{\partial\theta_i}(\Sigma_{C_\ell}^{-1})_{XY}^{\ell\ell'}\frac{\partial C_{\ell'}^Y}{\partial\theta_j} \tag{9}$$

$$= \frac{1}{C_\ell^{\rm fid}}\frac{\partial C_\ell}{\partial\theta_i} \cdot (\Sigma_{A_\ell}^{-1}) \cdot \frac{1}{C_\ell^{\rm fid}}\frac{\partial C_\ell}{\partial\theta_j} \tag{10}$$

$$\approx \frac{\partial A_b}{\partial\theta_i} \cdot (\Sigma_{A_b}^{-1}) \cdot \frac{\partial A_b}{\partial\theta_j}. \tag{11}$$

For ease of notation, we drop the summation symbols and transition to using matrix products in the second line. In the last line, we assume that the Fisher matrix is approximately equivalent to its binned version. We obtain the derivatives of A_b with respect to the cosmological parameters via a minimum-

Figure 5. Ratio of the ΛCDM parameter constraints derived from MUSE to those derived from the analytical covariance matrix for the SPT-3G Main survey (dark green-filled circle) and the SPT-3G Wide survey (orange-filled triangle). We note that they agree with each other within 10%.

variance (MV) binning of $\partial C_\ell / \partial \theta$ given by

$$\frac{\partial A_b}{\partial \theta} = \frac{1}{\sum_{\ell \in b} \frac{1}{\sigma^2_{A_\ell}}} \sum_{\ell \in b} \frac{1}{\sigma^2_{A_\ell}} \frac{\partial C_\ell / \partial \theta}{C_\ell^{\rm fid}}, \tag{12}$$

where we use an analytic ansatz for the weighting function $\sigma^2_{A_\ell}$. For $X \in [TT, EE, \phi\phi]$ this is given by

$$\sigma^2_{A_\ell^X} = \frac{\sigma^2_{C_\ell^X}}{(C_\ell^{X,\rm fid})^2} \equiv \frac{2}{2\ell + 1} \frac{(C_\ell^X + N_\ell^X)^2}{(C_\ell^{X,\rm fid})^2} \tag{13}$$

and for TE it is

$$\sigma^2_{A_\ell^{TE}} = \frac{1}{2\ell + 1} \frac{(C_\ell^{TE})^2 + (C_\ell^{TT} + N_\ell^{TT})(C_\ell^{EE} + N_\ell^{EE})}{(C_\ell^{TE,\rm fid})^2}. \tag{14}$$

In Figure 5, we show the ratio of parameter constraints obtained from MUSE and the analytic covariance for SPT-3G Main (green) and the SPT-3G Wide (orange) surveys. We find that these methods are consistent with each other within a 10% margin, which we deem sufficient to satisfy our validation criteria.

There are a number of reasons to expect these errors to differ to some degree, which we already brought up when describing the advantages of MUSE. Another reason is that the analytic results are not binned, but we found that for both the Wide and Main surveys, binning to $\Delta\ell = 100$ only leads to at most 2% degradation in constraints. The largest difference is the 8% tighter constraint on $\Omega_b h^2$ from the analytic forecast for the SPT-3G Wide survey. This is because the analytic estimate does not include the ℓ-by-ℓ lensing-induced correlations among different CMB multipoles, and that can lead to overly optimistic constraints. By artificially removing off-diagonal elements from the MUSE covariance matrix,[39] we were able to largely reproduce this reduced analytic error for both $\Omega_b h^2$ and n_s.

3.4. Combining with Planck Data

Comparison of the SPT-only ΛCDM constraints with those from Planck, as we will see, will enable a powerful test of the ΛCDM model. If these tests are consistent with ΛCDM, then

we will be interested in using the combined SPT-3G+Planck data to estimate ΛCDM parameters, as Planck provides complementary information on large angular scales. Consistent or not, we will also be interested in using the combined data to constrain ΛCDM extensions. Hence, we report the expected constraints from the combined data sets under the assumption of ΛCDM as well as under the assumption of various extensions.

The standard approach to obtain this combination is to add the Fisher matrices from SPT-3G and Planck similar to Equation (7) as

$$\mathcal{F}_{\rm SPT+Planck} = \mathcal{F}_{\widehat{\rm SPT}} + \mathcal{F}_{\widehat{\rm Planck}}, \tag{15}$$

where $\mathcal{F}_{\widehat{\rm SPT}}$ is the modified SPT-3G Fisher matrix obtained by taking the inverse variance combination of SPT-3G and Planck noise in the field under consideration; and $\mathcal{F}_{\widehat{\rm Planck}}$ is the modified Planck Fisher matrix after scaling to remove the overlapping sky region between SPT-3G and Planck. For example, if $f_{\rm sky} = 1$ for $\mathcal{F}_{\rm Planck}$, then for $\mathcal{F}_{\widehat{\rm Planck}}$, we use $f_{\rm sky} = 1 - f_{\rm sky}^{\rm SPT}$.

However, obtaining Equation (15) is nontrivial as it requires us to know the sky fraction used by Planck, which varies for different bands and power spectra (Planck Collaboration et al. 2020). Instead, we follow a different approach which involves two steps: first, we derive the Planck Fisher matrix directly from the publicly available Planck PR3 chains (Planck Collaboration et al. 2020); second, we combine the above Planck Fisher matrix with SPT-3G Fisher matrix, obtained using the analytic method. We modify the SPT-3G Fisher matrix by removing the large-scale modes from it, to avoid double counting information in the overlapping region.

We use BASE_PLIKHM_TTTEEE_lowL_lowE_lensing[40] chains for the first step unless specified otherwise. These chains, which contain samples from the probability distribution of cosmological parameters, are used to construct a parameter covariance matrix. By inverting this covariance matrix, we obtain the Planck Fisher matrix. For the second step, we restrict the information we use from SPT power spectra to multipoles above some $\ell_{\rm min}$ or $L_{\rm min}$ threshold, set by the approximate multipole at which the S/N for Planck is $\times 2$ lower than that for SPT in the same patch. We find that the choice of $\ell_{\rm min}$ does not change significantly for different SPT-3G surveys. As can be seen from Figure 6, which shows the ratio of Planck TT, TE, and EE power spectrum uncertainties to those projected for SPT-3G, this threshold is roughly 2000, 1000, and 750 for TT, TE, and EE, respectively, and we adopt these values for the joint forecasting. For lensing power spectra, we set $L_{\rm min} = 30$ (the same as our fiducial setting) because Planck's lensing S/N is much lower than SPT on all scales, as can be seen in Figure 3. However, we find our forecasts to be insensitive to the choice of $L_{\rm min}$. For example, with $L_{\rm min} = 400$ for SPT, our constraints only weaken by $\lesssim 5\%$.

We validate this approach of using $\ell_{\rm min}$ cuts rather than the $f_{\rm sky}$ scaling in Equation (15) by creating a toy model for a Planck-like Fisher matrix with $f_{\rm sky} = 0.5$. For this toy model, we use the following multipole ranges: $\ell \in [2, 2000]$, [30, 2000], [30, 2000], respectively, for TT, TE, and EE and $L \in [30, 400]$ for $\phi\phi$. Next, we compare the Fisher forecasts

---

[39] Specifically, we did this by inverting it, removing the off-diagonals, and inverting back.

[40] Planck chains are downloaded from https://wiki.cosmos.esa.int/planck-legacy-archive/index.php/Cosmological_Parameters.
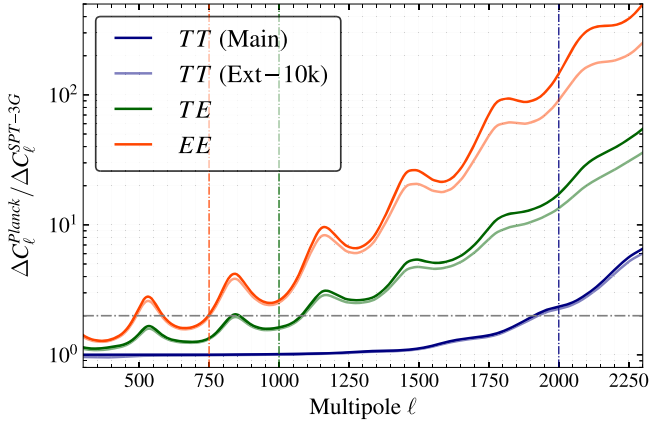
Figure 6. Ratio of power spectrum errors for Planck to those of SPT-3G for the same sky fraction. $\ell_{\min}$, the multipole value at which we switch from Planck to SPT-3G in combined constraints (shown as the vertical dashed–dotted lines), is chosen to be where this ratio roughly crosses 2. The blue, green, and orange colors correspond to TT, TE, EE, respectively. For $\phi\phi$, this ratio is greater than 2 for all the multipoles used in the forecast, and therefore it is not shown. The darker curves correspond to the SPT-3G Main survey, whereas the lighter curves represent the Ext-10k survey. The choice of $\ell_{\min}$ does not change significantly for different SPT-3G surveys.

from Equation (15) and the $\ell_{\min}$-cut approach discussed above. We find the results from the $\ell_{\min}$ cut approach to be $\lesssim 8\%$ worse than the traditional method. Given that the two methods agree well and given that our $\ell_{\min}$-cut-based forecasts are slightly on the conservative side, we choose to use this approach for the rest of this work.

4. Results

In this section, we begin by presenting our forecasts on cosmological parameters using all three SPT-3G surveys, assuming the six-parameter ΛCDM model. Subsequently, we project the extent to which combined SPT-3G and Planck data can constrain both single- and double-parameter extensions to the ΛCDM model. We also qualitatively investigate how well SPT-3G data can differentiate between ΛCDM and alternative models that have been proposed in the literature to address current cosmological tensions (for example, Cyr-Racine et al. 2022; Schöneberg et al. 2022; Meiers et al. 2023; Hughes et al. 2024; Khalife et al. 2024). The models we consider are fully consistent with current CMB and lensing power spectra measurements but make different predictions, from those of ΛCDM, for signals that can be measured well by SPT-3G.

4.1. Forecasts of Constraints on ΛCDM Parameters

We start first with forecasts of constraints on the six parameters of the ΛCDM model, namely, baryon density $\Omega_b h^2$, cold dark matter density $\Omega_c h^2$, Hubble constant H_0, optical depth to reionization $\tau_{\rm re}$, amplitude (defined at the pivot scale $k_0 = 0.05\,{\rm Mpc}^{-1}$), and spectral index of scalar fluctuations, A_s and n_s. For these constraints we fix the neutrino mass to the minimal value of 0.06 eV. We also include a prior on $\sigma(\tau_{\rm re}) = 0.007$ from Planck (Planck Collaboration et al. 2020). We use the MUSE approach as described in Section 3.3 to derive these constraints, and remind the reader that there is agreement between MUSE and the traditional analytic approach to better than 10%, as shown in Figure 5.

As we will see below, SPT-3G can produce constraints on ΛCDM parameters that are tighter than those we have from
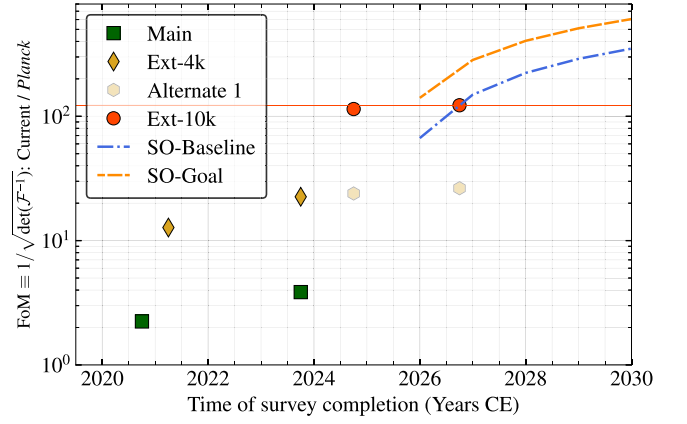
Figure 7. FoM for ΛCDM compared to Planck: we present the FoM for SPT-3G Main (green), Ext-4k (yellow), and Ext-10k (red). The transparent yellow circle represents the improvement in Ext-4k, if we were to continue the SPT-3G Main survey during 2024 as opposed to conducting the SPT-3G Wide survey. The evident increase in FoM with the new strategy emphasizes its potential efficacy over continuing the SPT-3G Main survey for cosmological parameter constraints. For reference, we also show the FoM expected for the two SO configurations (Baseline in blue and Goal in orange) under the assumption that the observations will begin in early 2025.

Planck. Since these constraints are obtained from largely different signals than those from Planck, they provide a robust consistency test for the ΛCDM model. As mentioned earlier in Section 3.4, we also present ΛCDM forecasts by combining SPT-3G and Planck.

In Figure 7, we present the projected figure of merit (FoM), which is inversely proportional to the volume of allowed six-dimensional ΛCDM parameter space. It is calculated as

$$\mathrm{FoM} = \sqrt{1/\det(\mathcal{F}^{-1})} \qquad (16)$$

for different SPT-3G surveys (SPT-3G Main in green, Ext-4k in yellow, and Ext-10k in orange-red) along with SO (blue). The FoM is inversely proportional to the six-dimensional volume of the 68% confidence region.[41] We plot it divided by the FoM for Planck.

As is evident from the figure, SPT-3G surveys significantly increase the FoM relative to that from Planck. From just the first 2 yr (2019–2020) of SPT-3G Main survey data, the FoM increases by $\times 2.5$ over Planck, and that jumps to $\times 13$ with the addition of the first 2 yr of SPT-3G Summer data. Both of these are further improved by roughly $\times 1.7$ with the inclusion of SPT-3G Main and SPT-3G Summer survey data through 2023.

The figure also demonstrates the benefit of expanding sky coverage rather than continuing to go deeper on the SPT-3G Main survey patch. One can see this from the minimal improvement to Ext-4k ($\times 1.1$) that we anticipate if we continue with the SPT-3G Main survey patch observations for the 2024 winter, indicated by the semitransparent yellow circle. On the other hand, switching to the SPT-3G Wide observations in the 2024 season improves the constraining power by $\times 5$ compared to Ext-4k and by $\times 130$ compared to Planck.

Were we to observe the SPT-3G Wide patch for one more year, we would not notice a significant increase in the FoM. Instead of doing this, we plan to switch back to the SPT-3G Main survey during the 2025 and 2026 winter seasons. Further

---

[41] In our Gaussian approximation, this proportionality holds independent of whether it is 68%, 95%, or any other such threshold for defining the confidence region.

Table 4
Forecasted 1σ Errors on ΛCDM Parameters for Various Survey Regions Using SPT Data

Parameter		SPT-3G Main	SPT-3G Summer	SPT-3G Wide	Ext-4k	Ext-10k
A_s	$[10^{-11}]$	2.79 (2.47)	2.66 (2.50)	2.54 (2.42)	2.53 (2.38)	2.35 (2.29)
$H_0[\text{km s}^{-1}\,\text{Mpc}^{-1}]$	$[10^{-1}]$	3.28 (3.16)	3.91 (3.47)	3.49 (3.26)	3.03 (2.95)	2.78 (2.78)
n_s	$[10^{-3}]$	7.23 (3.14)	6.12 (3.16)	5.10 (3.03)	4.76 (3.00)	3.66 (2.83)
$\Omega_b h^2$	$[10^{-5}]$	12.9 (7.87)	14.9 (8.68)	11.9 (7.66)	9.5 (6.7)	7.37 (5.67)
$\Omega_c h^2$	$[10^{-4}]$	8.86 (7.71)	9.84 (8.34)	8.92 (7.97)	8.07 (7.39)	7.36 (7.10)
τ_{re}	$[10^{-3}]$	6.85 (6.64)	6.78 (6.65)	6.59 (6.47)	6.63 (6.42)	6.28 (6.19)

Note. The numbers in the parentheses correspond to the constraints obtained when SPT-3G is combined with Planck. Note that when SPT-3G is combined with Planck, we remove information below $\ell_{\min} = 2000, 1000, 750, 30$ for *TT, TE, EE,* and $\phi\phi$ power spectra, respectively, from SPT-3G, to avoid double counting information.

noise reduction in the SPT-3G Main survey will not increase the FoM much, as can be seen in Figure 7, but will significantly improve the measurements of the secondary CMB anisotropies including lensing, which will further improve the subtraction of lensed B-modes, and hence, the search for B-modes from primordial gravitational waves (Ade et al. 2021).

In Table 4, we list our forecasts of ΛCDM parameter errors for different SPT-3G data sets. We also present them in Figure 8, where the bars show the ratios of the values of $\sigma(\theta)$ from Planck to those from SPT.

Let us begin by noting two things relevant to the interpretation of our A_s and τ_{re} results. First, the calibration of SPT-3G maps relies on data from Planck (Dutcher et al. 2021), and, consequently, SPT-3G constraints on the normalization parameter A_s are not entirely independent of Planck. Second, for SPT-only constraints in this work, we include a Planck-like prior on the optical depth, $\sigma(\tau_{re}) = 0.007$ since τ_{re} is primarily constrained by the large-scale $\ell \lesssim 10$ reionization bump in *EE/TE*, not accessible by SPT. All the τ_{re} constraints are dominated by this prior. These two points are not unrelated since the combination $A_s\, e^{-2\tau_{re}}$ is very tightly constrained by CMB data at $\ell > 20$, so improvements in τ_{re} determination translate into improvements in A_s determination, and vice versa. The small improvements that we do see in τ_{re} are due to the dependence of the amplitude of gravitational lensing on A_s, an amplitude unaffected by τ_{re}.

Focusing on the other four parameters, we find that the SPT-only constraints are generally comparable to, or better than, those obtained from Planck alone, for each of our three SPT-3G survey combinations. For the case of Ext-10k, the improvements in H_0 and $\Omega_b h^2$ are nearly a factor of 2, and for $\Omega_c h^2$ they are just more than a factor of 1.5. For n_s, the relative errors from the SPT-3G Main survey and Ext-4k survey are larger compared to those from Planck due to Planck's significantly broader multipole range. Nonetheless, the Ext-10k survey still manages to achieve slightly tighter constraints on n_s than what we have from Planck.

4.1.1. Comparison with SO

In Figure 7, we also show the expected constraining power from the Simons Observatory for two configurations: SO-Baseline (blue dashed–dotted) and SO-Goal (orange dashed–dotted), based on the noise levels in Simons Observatory Collaboration (2019). We use the original SO noise model code[42] to get the noise curves for the individual frequency bands and combine information from all the bands using the
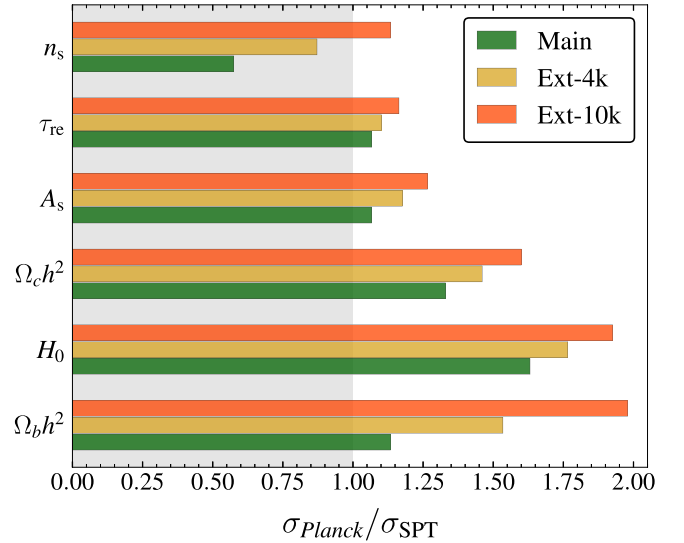
Figure 8. Constraints on the standard ΛCDM parameters expected from the three SPT surveys (SPT-3G Main in green, Ext-4k in yellow, and Ext-10k in red) compared to Planck (gray-shaded region). We expect significant improvements on all the parameters except n_s and τ_{re}, which depend on the largest scales that ground-based surveys cannot easily measure.

LC technique described in Section 3.1. We use the same multipole ranges described in Section 3.2 for forecasting constraints from SO. As a check, we compare the constraints that we get from our forecasts for SO against what is reported in Simons Observatory Collaboration (2019) but note that we do not include Planck unlike SO's original forecasts.

Comparing our forecasts for SO to Table 3 of the Simons Observatory Collaboration (2019), our forecasts are slightly better for H_0 and $\Omega_c h^2$ but they agree within 10%. For n_s and $\Omega_b h^2$, we obtain 15%–35% worse constraints, which is presumably because we do not add the large-scale information from Planck. On the other hand, we obtain roughly 35% (20%) better constraints on A_s (τ_{re}). When we increase the prior uncertainty on optical depth to $\sigma(\tau_{re}) = 0.009$ to match SO's forecasting code (see caption of Table 3 in Simons Observatory Collaboration 2019), our results on A_s and τ_{re} match the numbers quoted in Simons Observatory Collaboration (2019). Switching to SO-Goal configuration reduces the errors on all parameters by 5% except for $\Omega_c h^2$, where the constraining power improves by 15%.

We also note from Figure 7 that the constraining power of the SPT-3G Ext-10k survey for ΛCDM parameters will be roughly similar to the first 2 yr of SO-Baseline. Such similar levels of constraining power between SPT and SO along with

significant sky overlap (see Figure 1) will allow for comparisons of the two data sets at both the power spectrum and map level (such as the ACT-Planck and SPT-Planck comparisons shown in Louis et al. 2014 and Hou et al. 2018) which will provide useful opportunities for identifying and/or limiting systematic errors in individual data sets.

4.1.2. Real-world Effects

In this section, we examine how our forecasts change as we vary our baseline modeling assumptions, and introduce additional nonideal aspects into our model of the data on which the forecasts are based. We modify our noise curves to account for filtering effects and to include a higher level of complexity in the noise due to the correlated atmospheric signal on large scales in the temperature data. We also investigate the degradation in constraints that could come from galactic foregrounds. We also check the impact of including uncertainties in the calibration of our temperature and polarization maps. As detailed below, we find the degradation of parameter errors relative to the baseline case, from all of these effects, is ≲10%. Finally, we build further confidence in our forecasts by comparing them to constraints from an ongoing MUSE analysis of the 2-yr SPT-3G Main data.

Atmospheric noise—The first thing we examine is the impact of the filtering applied to the detector time-ordered data (TOD) before it is processed into maps. To avoid excess noise in the scan direction in the resulting maps, primarily as a result of the large-scale atmospheric noise, we apply filters to remove the long-timescale information from the detector TOD. While this improves the quality of the maps, it results in a reduction of data volume that increases the final power spectrum errors by a factor equivalent to raising map noise levels by roughly 10%. We test the impact of this by increasing the white noise levels in Table 1 by 10%. We found that this results in changes to the parameter constraints at the ≤1% level. Second, since SPT-3G uses multichroic detectors that can simultaneously observe in multiple frequencies, the large-scale atmospheric noise is expected to be correlated between bands. From the 2019–2020 data set, we estimate the correlation at the largest scales to be ∼90% between the 150 and 220 GHz bands, and around 70% between the 90 and 150 GHz bands as well as between the 90 and 220 GHz bands. This degree of correlation diminishes as we move to small scales. To take this into account, we set the cross-frequency noise to be correlated across bands and rerun the LC step to get the residuals. This correlated noise, in fact, reduces the large-scale LC residuals slightly. When we propagate these to parameter constraints, we find changes to the parameter constraints at the ≤1% level, indicating that our forecasts are robust to these details about the noise spectra.

Galactic foregrounds and mask—Given that the SPT-3G Wide survey extends close to the plane of the galaxy (see Figure 1), it is crucial to understand the impact of galactic foregrounds on the parameter constraints. To assess this, we make use of the PySM simulations (Thorne et al. 2017) of galactic foregrounds and the galactic foreground masks (GAL070, GAL080, GAL090) produced by the Planck Collaboration (Planck Collaboration et al. 2016b). The names of the above masks correspond to the sky retained after masking the galactic plane. For instance, GAL090 masks 10% of the region with a high level of foregrounds close to the

galactic plane, while GAL070 removes 30% of the sky and is the most conservative among the three.

We use these masks and calculate the level of galactic dust and synchrotron signals in PySM simulations in the following regions: Case (A) GAL080-GAL070; Case (B) GAL090-GAL070; and Case (C) GAL090-GAL080. The three cases correspond to the differences between the respective masks; for instance, GAL080-GAL070 represents the sky area included in mask GAL080 but excluded in GAL070. As expected, we find the galactic foreground in Case (C) to be the highest followed by Cases (B) and (A).

We perform a conservative test by assuming that the galactic foreground levels across the entire SPT-3G Wide survey match one of these three cases. With this assumption, we derive the LC residuals and the subsequent impact on the parameter constraints. Even for Case (C), where the galactic foregrounds are the highest, we find the constraints degrade by only 8%. This is not surprising given that the galactic foregrounds are mostly important on the largest scales and the constraining power of SPT-3G is predominately driven by the high-ℓ region.

In the preceding sections, we mentioned that the observing strategy to minimize galactic foreground contamination in the SPT-3G Wide involves observing within the confines of the Planck GAL080 mask, which corresponds to roughly 6000 $\deg^2$ of sky coverage. In the scenario where we might need to adopt a more conservative Planck GAL070 mask, we found that this would lead to a modest degradation in parameter constraints, at 4%–5%. While we do not address potential biases due to mismodeling of the galactic foregrounds, we remain confident that any such biases would be minimal, given that the levels of galactic foregrounds are significantly lower than the CMB power spectra levels at the multipoles relevant to this analysis.

Temperature and polarization calibration—Next, we assess the impact of calibration uncertainty on the temperature and polarization maps by including two absolute calibration parameters, T_{cal} and P_{cal} (as defined in Dutcher et al. 2021), in our forecasts and marginalizing over them. In the case where we do not apply a prior, we find a significant ×2 hit on some of the parameters, which is not surprising since parameters like A_s are fully degenerate with the calibration parameters. By comparing SPT-3G Main survey maps from 2019–2020 to Planck maps in that same region, we are able to constrain T_{cal} and P_{cal} to roughly 0.2% and 1%, respectively (where the errors are a combination of statistical uncertainty in the comparison and uncertainties in the Planck calibration). If we adopt these as priors, the resulting degradation in the parameter constraints is ≤5% for all parameters. If we loosen the T_{cal} prior to 1%, the degradation increases to ∼20%. If we assume either parameter is estimated perfectly and allows for uncertainty in only one calibration parameter, we find the resulting degradation to be negligible, even without any prior, consistent with the results from Galli et al. (2021).

Finally, we replace the covariance matrix for the 2 yr SPT-3G Main survey from this work with the one from an ongoing MUSE analysis performed on the real data from the same survey. The latter takes into account certain effects that are present in the real data but not taken into account in our forecasts. These include anisotropic noise, anisotropic filtering, and masking. With this covariance swap, we find that the degradation in the parameter constraints is ≤10%.
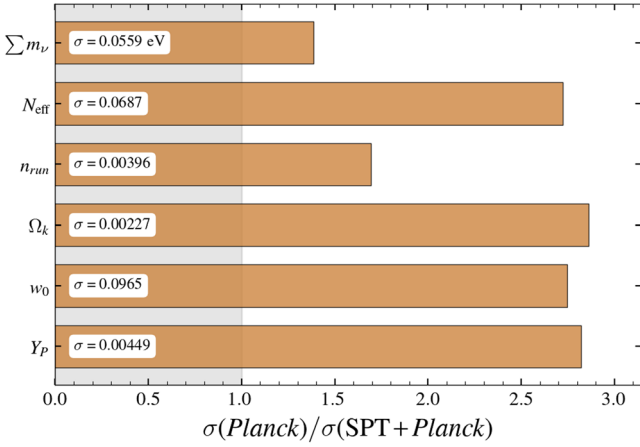
Figure 9. Ratio of 1σ constraints on single-parameter extensions from Planck to those forecasted from the combination of Ext-10k and Planck. The gray-shaded region corresponds to the current best constraints from Planck alone. The actual errors are expressed in the text boxes.
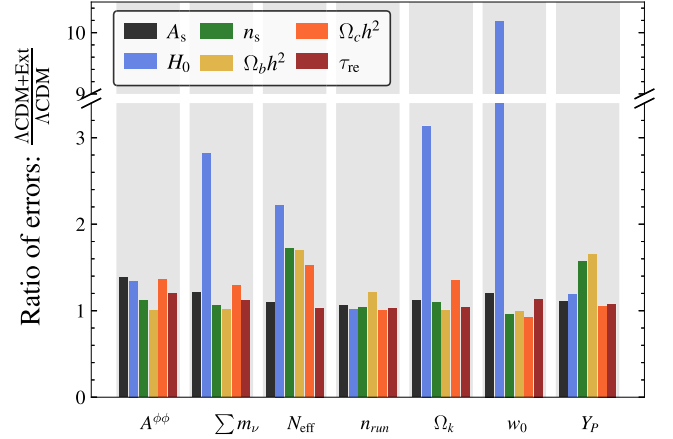

Figure 10. Degradation in the ΛCDM constraints due to single-parameter extensions compared to the original constraints reported in Figure 8 for the Ext-10k+Planck data set. The horizontal axis shows the parameter that is varied in our extensions. Except for H_0, which is affected by a geometric parameter degeneracy, the degradation in constraints for other ΛCDM parameters is quite mild.

4.2. Single-parameter Extensions to ΛCDM

Now we turn our attention toward extensions to the ΛCDM model. For extensions, we always combine SPT-3G with Planck, and use the analytic method. We consider seven different cases by varying the following parameters one at a time along with the six ΛCDM parameters: dark energy equation of state (w_0), helium mass fraction (Y_P), running of the spectral index ($n_{\rm run} \equiv \mathrm{d}n_s/\mathrm{d}\ln k$), sum of neutrino masses ($\sum m_\nu$), effective number of neutrino species ($N_{\rm eff}$), and the spatial curvature parameter (Ω_k). The forecasted constraints for Ext-10k are reported in Figure 9. As before, we show the improvement in constraints compared to Planck using the bars. The actual parameter constraints are given in the text boxes. The constraints from other SPT-3G surveys are presented in Table 5 of Appendix B.

We find a significant ($\times 2 - \times 3$) reduction of the errors in many of these parameters, namely, Ω_k, w_0, Y_P, and $N_{\rm eff}$. For other parameters, namely, $\sum m_\nu$, and $n_{\rm run}$, the improvement is $\times 1.4 - \times 1.7$ compared to Planck. Some of these improvements are driven by the inclusion of lensing (Ω_k, w_0), while others come from higher-redshift information in the damping tail of the CMB, whose extraction benefits from wide sky coverage ($n_{\rm run}$, Y_P, and $N_{\rm eff}$).

We also investigate the degradation in ΛCDM constraints due to degeneracies with the extension parameters. We present these error degradations in Figure 10 for Ext-10k+Planck; the full list can be found in Table 6 of Appendix B. As can be inferred from the figure, the constraints on the Hubble constant H_0 degrade significantly when we free $\theta \in [\sum m_\nu, N_{\rm eff}, \Omega_k, w_0]$. Note that these degradations largely disappear with the addition of external data sets that constrain the redshift-distance relationship down to $z \lesssim 0.1$, namely, supernova brightness measurements. This is the reason why these extensions are not viable solutions to the H_0 tension (Knox & Millea 2020). The degradation is less severe ($\sim \times 1.6$) for n_s, $\Omega_b h^2$ when we vary $\theta \in [N_{\rm eff}, Y_P]$. For the rest, the constraints are robust and the degradation is $\lesssim \times 1.3$.

In expanding the parameter space from ΛCDM to ΛCDM+w_0, we notice an unexpected tightening in the constraints for parameters $\Omega_b h^2$, $\Omega_c h^2$, and n_s. We suspect that this arises from our use of a Gaussian approximation for a posterior that is significantly non-Gaussian. The non-

Gaussianity is visually evident in the one and two-dimensional marginal posteriors derived from the appropriate Planck chains. With the addition of an H_0 prior, the range of acceptable w values tightens significantly, reducing the degree of non-Gaussianity, and this anomalous behavior of our forecasts no longer appears.
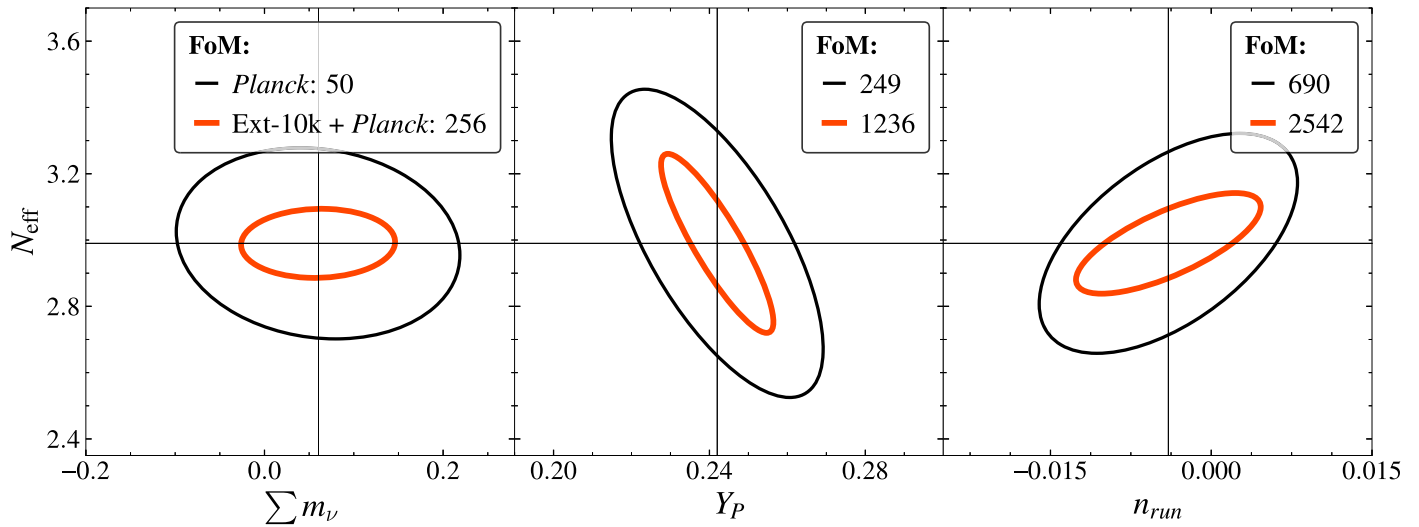
4.3. Double-parameter Extensions to ΛCDM

We also explore two-parameter extensions similar to those considered in Planck Collaboration et al. (2020). These are (a) $N_{\rm eff}$ and Y_P, (b) $N_{\rm eff}$ and $n_{\rm run}$, and (c) $N_{\rm eff}$ and $\sum m_\nu$. In Figure 11, we present the marginalized two-dimensional contours for the above extensions from both Planck (black) and Ext-10k+Planck (orange). The FoM for the two-parameter extensions, calculated similarly to Figure 7, is given in the legend. In most cases, we find an improvement of greater than a factor of 2 relative to Planck alone.

In Case (A), we vary the effective number of neutrino species $N_{\rm eff}$ and the fraction of baryonic mass in helium Y_P simultaneously. Such constraints are useful for constraining scenarios in which the value of $N_{\rm eff}$ at Big Bang nucleosynthesis differs from that at recombination (Millea et al. 2015; Cyburt et al. 2016; Particle Data Group et al. 2020). Since both these parameters affect the damping tail of the CMB, they are partially degenerate, and as expected, the constraints on both these parameters degrade by more than $\times 2$ compared to the single-parameter extensions in Figure 9.

In Case (B), we vary $N_{\rm eff}$ and $n_{\rm run}$, which are also degenerate to some level leading to $\times 1.5$ weaker constraints compared to Figure 9.

In Case (C), we vary $N_{\rm eff}$ and the sum of neutrino masses $\sum m_\nu$ since one can expect some level of correlation between the two (Planck Collaboration et al. 2020). However, this correlation depends on the data sets being considered. In our case, $\sum m_\nu$ is primarily constrained by lensing, while $N_{\rm eff}$ constraints are dominated by the small-scale TT, EE, and TE power spectra. Subsequently, the degradation in the constraints on these two parameters is negligible compared to what we obtain for the single-parameter extensions in Figure 9.

Figure 11. Marginalized two-dimensional parameter contours for the three pairs of double-parameter extensions to ΛCDM considered in this work. The red contours represent the joint constraints from the Ext-10k+Planck, and the black contours show the constraints from Planck alone. The inverse of the allowed volume of the two-dimensional parameter space (FoM) is given in the legend. Compared to the constraints from Planck alone, we find reductions in individual parameter errors that approach or exceed a factor of 2 except for n_{run}, where we obtain a ×1.3 reduction.

5. Power Spectrum Predictions from ΛCDM and Alternatives

In this section, we discuss, in a qualitative manner, prospects for using SPT-3G data to detect departures from ΛCDM predictions for CMB power spectra conditioned on Planck data. Many alternative models that resolve cosmological tensions, such as the H_0 and σ_8 tensions, predict power spectra that differ from ΛCDM predictions at small angular scales, and we use a selection of such models to guide our discussion. In Figure 12, we present the ΛCDM predictions for angular power spectra given Planck data, the predictions of alternative models that fit the Planck data well while either having a high H_0 or a low σ_8, and the forecasted Ext-10k error bars.

The selected alternative models are (a) a phenomenological model of nonperturbatively modified recombination (ModRec; Lynch et al. 2024); (b) an atomic dark matter (ADM) model arising from a hidden dark sector charged under a U(1) gauge interaction (Hughes et al. 2024); and (c) a model featuring an additional dark fluid with an equation of state parameter that is a free function of redshift, hereafter "high-dimensional generalized dark matter" (HDGDM. Meiers et al. 2023).

We present one set of spectra from each of these models in Figure 12 as a relative shift $\Delta C_\ell^X = C_\ell^X - C_{\ell,\mathrm{ref}}^X$ compared to the reference ΛCDM mean Planck $C_{\ell,\mathrm{ref}}^X$, normalized as described in the figure caption. Here, X corresponds to one of the primary lensed CMB $TT/EE/TE$ or the lensing $\phi\phi$ power spectra. Each of these spectra is drawn from posterior distributions conditioned on Planck and baryon acoustic oscillation (BAO) data, although the HDGDM spectra also include uncalibrated supernovae data in the fit. It should be noted that the specific BAO data sets used in these constraints differ: please see the appropriate references for details.

The left-hand panels of Figure 12 show these spectra in relation to existing CMB measurements from Planck, SPTpol (Bianchini et al. 2020), SPT-3G 2018 (Dutcher et al. 2021), and ACT DR6 (Qu et al. 2024). For angular scales that have been probed by multiple experiments, only the most constraining data set has been plotted. This set of panels highlights that although these models make predictions that differ from

ΛCDM, they are currently not ruled out by the data. To the right, we show the 68% confidence region for angular power spectrum predictions conditioned on Planck data and assuming ΛCDM, along with forecasted band power errors for Ext-10k in black.

The Planck data, along with the assumption of ΛCDM, make tight predictions for the power spectrum residuals even at angular scales not probed by Planck. This is evident from the right-hand panels of Figure 12, where the gray confidence interval extends to no more than about 2% for the TT, TE, and EE power spectra. This range represents the expected region that the power spectra observed by SPT-3G will fall in if measurements continue to be consistent with ΛCDM. As is evident in these panels, the alternative models presented here exhibit deviations, which are larger than this expected range, and larger than the expected precision of SPT-3G. We now discuss each of these models in turn.

The potential role of changes to recombination in alleviating the H_0 tension has been explored in Chiang & Slosar (2018), Hart & Chluba (2020a), Sekiguchi & Takahashi (2021), Lee et al. (2023), and Cyr-Racine et al. (2022). Physical models which have a modified recombination epoch include models with varying fundamental constants (Ade et al. 2015; Hart & Chluba 2018, 2020b; Sekiguchi & Takahashi 2021), primordial magnetic fields (Jedamzik & Pogosian 2020; Galli et al. 2022; Rashkovetskyi et al. 2021), or energy injection from decaying dark matter (Galli et al. 2013; Slatyer & Wu 2017; Finkbeiner et al. 2012). The ModRec model presented here is an extension of ΛCDM that allows for a purely phenomenological modification of the ionization fraction as a function of redshift through the epoch of hydrogen recombination, in order to study the role of these changes independently of the details of particular physical models. We note that the different modified ionization fractions predicted by the above physical models can be well approximated within the ModRec model using seven parameters characterizing deviations from the standard recombination scenario.

This additional freedom allows for higher values of H_0 to provide good fits to the Planck data. The ModRec model accommodates a high value of H_0 by altering the recombination process, shifting last scattering to higher redshifts, and
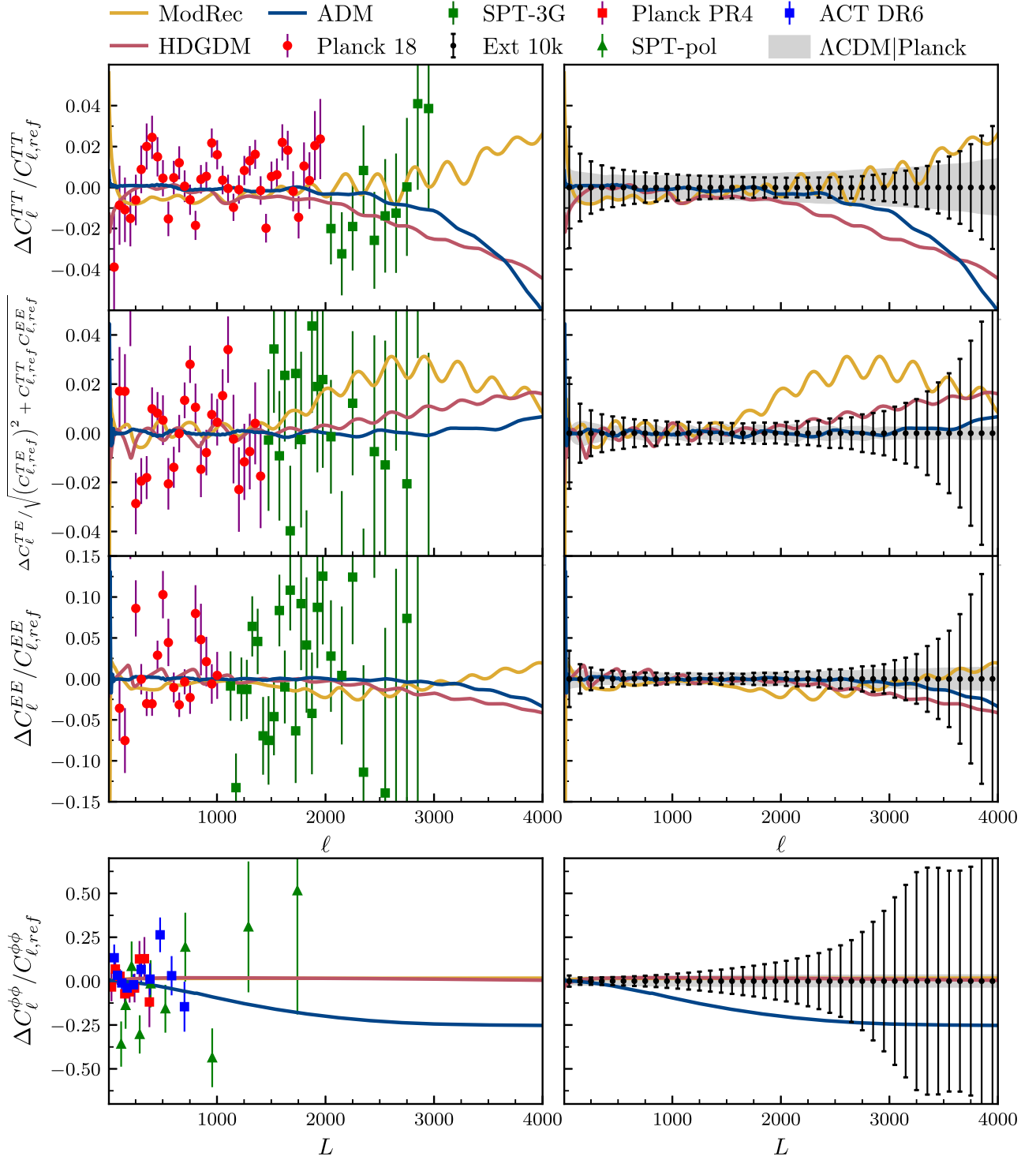
Figure 12. Left panels: current data from CMB experiments and some alternative models with either higher H_0 or lower σ_8 (see the text). Except for lensing data, only the most constraining observations in a given multipole range have been plotted for clarity. Each spectrum has the best-fit ΛCDM spectrum given Planck subtracted as a reference and is normalized in an ℓ-dependent manner to reduce dynamic range, as described in the y-axis label. Note that for the ADM model, neither the model prediction nor the reference model includes nonlinear corrections to the lensing power spectrum, as existing nonlinear correction procedures do not account for the modified dark sector physics. All spectra are taken from chains constrained using Planck and BAO data, but the specific BAO data sets used differ between models. The HDGDM constraints also used uncalibrated supernovae data as well as the SH0ES H_0 measurement. Right panels: the same models as in the left panels, forecasted band power errors for Ext-10k, and the 68% confidence region given Planck and the assumption of ΛCDM. The band power errors have been binned with $\Delta\ell = 100$. Note that the ΛCDM predictions conditioned on Planck are very tight, even in regions where Planck data on their own are completely unconstraining.

increasing the width of the visibility function. This reduces the comoving size of the sound horizon at recombination, so that the shorter distance to last scattering associated with a higher H_0 does not shift the well-determined angular size of the sound horizon. It also impacts the damping scale, an effect ameliorated by the change to the visibility function width.

In Figure 12, we show predictions within the ModRec model for a set of parameters that fit Planck and eBOSS BAO data at

least as well as a ΛCDM best fit, while having $H_0 = 70.48 \,\mathrm{km\,s^{-1}\,Mpc^{-1}}$. To maintain the fit with Planck data, residuals with respect to the fiducial cosmology get shifted to higher multipoles, which, while unprobed by Planck, are expected to be measured with high S/N by SPT-3G. We see that SPT-3G has clear potential to rule out such a model, particularly through measurements of the TE spectrum. We note that without including BAO data, much higher values of H_0 are achievable within the ModRec model while staying consistent with Planck. In this case, if SPT-3G measurements remain consistent with ΛCDM, solutions to the H_0 tension that modify recombination will be seriously challenged by CMB data alone.

Another approach to resolving the H_0 tension is to leave the recombination history unmodified and to instead introduce more freedom in the dark sector. The HDGDM model is another phenomenological model that uses the generalized dark matter (GDM) model of Hu (1998) and allows the equation of state parameter for the GDM to be an arbitrary function of redshift. Meiers et al. (2023) used such a model to approximate, and perturb around, a more physical model, the "step-like" model of Aloni et al. (2022). These authors introduce a massive particle that becomes nonrelativistic before decaying, in equilibrium, into a massless final state. The equation of state parameter $w(z)$ for such a species begins at one-third, drops as the particle becomes nonrelativistic, and returns to one-third in the final massless state. This new component affects the expansion history in a nontrivial way, and alters the time-dependent gravitational driving of the plasma. They found that a transition at $z \sim 20,000$ could accommodate a higher H_0. In Figure 12, we present the best-fit spectrum of the "step-like restricted" model of Meiers et al. (2023) constrained using the "$\mathcal{D}+$" data combination in that work, which includes Planck BAO, uncalibrated supernovae data, as well a Gaussian likelihood centered at the SH0ES measurement $H_0 = 73.04 \pm 1.04 \,\mathrm{km\,s^{-1}\,Mpc^{-1}}$ (Riess et al. 2022). This model has $H_0 = 71.88 \,\mathrm{km\,s^{-1}\,Mpc^{-1}}$, illustrating how the HDGDM model can accommodate higher values of H_0. However, the TT damping tail predictions from this model differ from the ΛCDM prediction using the Planck mean parameters at more than 2% for $\ell > 3000$, which should be distinguishable with SPT-3G.

In addition to the H_0 tension, in recent years, there has been increased attention to the potential discrepancy between different measurements of the amplitude of matter fluctuations on $8h^{-1}\,\mathrm{Mpc}$ scales, σ_8. Inferences from Planck, that depend on assuming the ΛCDM model, give a value of $\sigma_8 = 0.811 \pm 0.006$, whereas the KiDS-1000 survey, measuring cosmic shear, gives a value of $\sigma_8 = 0.76^{+0.025}_{-0.020}$ (Planck Collaboration et al. 2020; Heymans et al. 2020). Although, DES sees less of a σ_8 tension compared to KiDS (Dark Energy Survey and Kilo-Degree Survey Collaboration 2023). In the ADM model considered here, this tension is addressed through the introduction of two dark fermions interacting with a dark photon, where the dark fermions make up some fraction f_{ADM} of the dark matter. This results in dark sector dynamics analogous to the dynamics of the baryon-photon plasma. The pressure support from the dark photon at early times, prior to the formation of dark atoms, suppresses the growth of structure. In general, this leads to effects in the CMB power spectra observable by Planck but if the dark sector temperature is cool enough, the epoch of significant dark photon pressure support

is early enough, and the Planck observables are relatively unaffected. More direct inferences of σ_8 are impacted by smaller scales than those to which Planck is sensitive; so, at the right dark photon temperature with a suppressed σ_8, Planck observables are unaffected. In Figure 12, we present the best-fit model identified in Hughes et al. (2024), coming from a region of parameter space consistent with Planck data, with $\sigma_8 = 0.7869$, a low dark photon temperature, and high f_{ADM}. For this fit, both CMB data from Planck were used, as were BAO measurements (see Hughes et al. 2024 for details).

From this survey of alternatives to ΛCDM, we conclude that measurements of temperature, polarization, and lensing power spectra from SPT-3G are capable of clarifying existing cosmological tensions.

6. Conclusions

We presented forecasts of constraints on cosmological parameters that can be derived from the estimates of lensing, temperature, and E-mode polarization power spectra to come from completed and ongoing SPT-3G sky surveys. We made forecasts for three combinations of the three SPT-3G surveys of varying sizes and depths, with particular emphasis on the combination of all three of these surveys, called Ext-10k, covering $\sim$10,000 deg^2 (25% of the sky). We showed that SPT-3G will enable some powerful tests of the ΛCDM model.

We showed that the constraining power of the full SPT-3G data set will surpass that of Planck for the power spectra at modes $\ell \gtrsim 1800$ in TT, $\ell \gtrsim 800$ in TE, at $\ell \gtrsim 450$ for EE, and at $L \gtrsim 30$ in $\phi\phi$. We calculated the predictions of the ΛCDM model, conditioned on Planck data, and found that they are highly precise in the power spectra on these scales, setting us up for a powerful test of ΛCDM.

We also demonstrated that SPT-3G will facilitate testing of the ΛCDM model at the level of cosmological parameters. By propagating the uncertainties on power spectra to uncertainties on cosmological parameters, our analysis suggests that data from SPT-3G will be able to achieve similar, or in some cases, tighter constraints than those from Planck. Since these constraints incorporate higher weights from polarization, from small angular scales in temperature, and from lensing when compared to those from Planck, a consistency check between the two will be a powerful test of ΛCDM. The constraints on the current expansion rate (H_0) and baryon density ($\Omega_b h^2$) improve by roughly a factor of 2 when compared with the constraints from Planck, while for the dark matter density ($\Omega_c h^2$), the improvement is a factor of 1.5. We find that the full SPT-3G data set is expected to achieve an improvement in the ΛCDM FoM of 130; i.e., SPT-3G will reduce the allowed six-dimensional parameter volume by a factor of 130 compared to Planck.

This reduction in volume is comparable to what is expected from the first two years of the SO-Baseline data set. This similarity in constraining power, plus the substantial amount of overlap in sky coverage, provides an opportunity for significant map-level consistency tests. These can be used to detect or limit sources of systematic error, increasing the robustness of the parameter determinations from both SO and SPT-3G.

We also explored how well we can test ΛCDM by forecasting constraints on single- and double-parameter extensions with the combination of Planck+SPT-3G. We found that the combined data will result in considerable improvements over Planck alone. For example, we found that the constraints

on single-parameter extensions improve by more than $\times 2$ for $\theta \in [\Omega_k, N_{\rm eff}, w_0, Y_P]$ and roughly $\times 1.5$ for $\theta \in [n_{\rm run}, \sum m_\nu]$ compared to Planck-only constraints. We also showed that including these extensions does not significantly degrade the constraints on the ΛCDM model parameters, except for H_0, which is highly degenerate with some of the extensions like w_0.

In addition to showing the highly precise predictions of the ΛCDM model on angular scales to be measured by SPT-3G, we showed that there are also alternative models that are consistent with current data, with significantly different predictions on these same angular scales. We considered three different models that could address existing cosmological tensions. While all of these models are consistent with Planck data, they exhibit deviations from the ΛCDM prediction deviations that are larger than the forecasted SPT-3G error bars. This set of alternative models illuminates the potential discovery space of SPT-3G observations.

These SPT-3G tests of ΛCDM will begin soon and then improve in precision over the next 5 yr. Later this year, we expect to release the first cosmological constraints from the first 2 yr of the SPT-3G Main survey observations, and soon afterward, from the first 2 yr of the Ext-4k survey. We forecast that this early data set will offer constraining power on the ΛCDM model parameters that is comparable to that achieved by Planck, improving the ΛCDM FoM by a factor of 2 (SPT-3G Main) and 13 (Ext-4k) relative to Planck. A significant portion of the SPT-3G Wide survey has already been completed and we could expect Ext-10k results as early as sometime in 2025.

Appendix A
Derivation of the MUSE Covariance Matrix

In the context of parameter inferences from CMB data, the observed maps (x), do not depend just on cosmological parameters (θ) but also on unobserved latent variables (z) such as the unlensed CMB field and the lensing potential field. In such a scenario, the likelihood ($\mathcal{L}(x|\theta)$) involves marginalizing the joint likelihood $\mathcal{L}(x, z|\theta)$ over the latent space.

$$\mathcal{L}(x|\theta) = \int d^N z \mathcal{L}(x, z|\theta) = \int d^N z \mathcal{L}(x|z, \theta) \mathcal{L}(z|\theta), \quad (A1)$$

where $\mathcal{L}(z|\theta)$ represents the likelihood of the unlensed CMB field or the lensing potential z, given a set of cosmological parameters θ. For parameter inferences, we are often interested in the gradient of this marginal likelihood, a quantity called the marginal score s_i.

$$s_i(\theta, x) \equiv \frac{d}{d\theta_i} \log \mathcal{L}(x|\theta). \quad (A2)$$

However, performing the integral over the maps of unlensed CMB and lensing potential, which contain an order of a million pixels, is a computationally challenging task and analytic solutions only exist for the simplest cases. MUSE gets around this problem by approximating the marginal score. The key ingredient of the MUSE score is a quantity referred to as $s^{\rm MAP}$, which is the gradient of the joint likelihood evaluated at the maximum a posteriori (MAP) estimate of the unlensed CMB field and the lensing potential, $\hat{z}_{\theta,x} \equiv \underset{z}{\rm argmax} \log \mathcal{L}(x, z|\theta)$

$$s_i^{\rm MAP}(\theta, x) \equiv \frac{d}{d\theta_i} \log \mathcal{L}(x, \hat{z}_{\theta,x}|\theta) \quad (A3)$$

and the MUSE score is defined as

$$s_i^{\rm MUSE}(\theta, x) \equiv s_i^{\rm MAP}(\theta, x) - \langle s_i^{\rm MAP}(\theta, x') \rangle_{x' \sim \mathcal{P}(x'|\theta)}, \quad (A4)$$

where the second term is calculated by averaging over simulations x' drawn from a probability distribution generated at the specified value of θ. Once we have the MUSE score, we can define an estimator for the band powers θ as the root of the equation $s_i^{\rm MUSE}(\theta^{\rm MUSE}, x) = 0$ and the band power covariance can be constructed by two related matrices, J and H, defined as

$$J_{ij} = \langle s_i^{\rm MAP}(\theta^*, x) s_j^{\rm MAP}(\theta^*, x) \rangle_{x \sim \mathcal{P}(x|\theta^*)}$$
$$- \langle s_i^{\rm MAP}(\theta^*, x) \rangle \langle s_j^{\rm MAP}(\theta^*, x) \rangle_{x \sim \mathcal{P}(x|\theta^*)}$$
$$H_{ij} = \frac{d}{d\theta_j} [\langle s_i^{\rm MAP}(\theta^*, x) \rangle_{x \sim \mathcal{P}(x|\theta)}] \bigg|_{\theta = \theta^*}. \quad (A5)$$

J is the covariance of the MAP gradients at the true value of band powers θ^*. We use simulations of the data in order to calculate this quantity. H can be thought of as the response matrix of the MAP gradients with respect to small changes in parameters that generate the simulated data. The band power covariance is constructed as follows:

$$\Sigma_{ij}^{\rm MUSE} \equiv \langle \Delta\hat{\theta}_i^{\rm MUSE} \Delta\hat{\theta}_j^{\rm MUSE} \rangle = (H^{-1} J H^{-1\dagger})_{ij}. \quad (A6)$$

A.1. Simulations

We create simulations of the data, which consists of the lensed CMB along with noise as described in Table 1. Utilizing

the best-fit Planck '15 spectrum, we produce a suite of 1000 flat-sky realizations of unlensed T, Q, and U CMB maps on a 512×512 pixel grid, spanning an area of $300\ \mathrm{deg}^2$, which are subsequently lensed by the lenseflow algorithm (Millea et al. 2019). We do not simulate the entire observation patch to limit the computational cost, thereby allowing us to run a large number of simulations. We do not expect this to have a significant impact as lensing is a local operation and the induced deflections are coherent only across a few degrees. Subsequently, we scaled this covariance matrix using an appropriate factor that corresponds to the ratio between our survey area and the simulated patch size. For the purposes of this forecast, we use a simplified version of the data model, which will be used in the actual analysis, whereby we ignore the effect of masking and filtering as is generally done with traditional fisher forecasts. We do not anticipate these to have a significant impact on the parameter constraints.

The data model used in this work can be written as

$$d = \mathbb{F} \cdot \mathbb{B} \cdot \mathbb{L}(\phi)f + n$$
$$f \sim \mathbb{C}_f(\boldsymbol{C}_\ell^{\mathrm{TT/TE/EE}})$$
$$\phi \sim \mathbb{C}_\phi(\boldsymbol{C}_\ell^{\phi\phi})$$
$$n \sim \mathbb{C}_n(N_\ell),$$

where d is the data; f is a Gaussian realization of the unlensed CMB map; ϕ is a Gaussian realization of the gravitational-lensing potential; $\mathbb{L}(\phi)$ is a linear lensing operator acting on f; $\mathbb{B}$ is the instrumental beam function; $\mathbb{F}$ is a mid-pass Fourier filter that cuts off ℓs below 300 and above 3500 (4000) for TT, TE (EE), and N_ℓ is the white$+1/f$ noise power spectrum as defined in Table 1.

A.2. Effective Lensing Reconstruction Map Noise

The effective lensing reconstruction noise is defined such that for an unbiased estimate of the lensing potential harmonic coefficients, $\hat{\phi}_{\mathrm{LM}}$, the per-mode variance of the residual to the true ϕ map is

$$N_L^{\phi\phi} = \langle (\hat{\phi}_{\mathrm{LM}} - \phi_{\mathrm{LM}}^{\mathrm{true}})^2 \rangle. \tag{A7}$$

For the quadratic estimate, for example, this is given by the sum of the N^0, N^1, $N^{3/2}$, etc. noise bias terms (Hu & Okamoto 2002; Madhavacheril et al. 2020). Note that if one has a biased estimate of the lensing potential, $\bar{\phi} = A\phi + n$ with some unknown normalization bias, A, and effective noise, n, the noise power can be written as

$$N_L^{\phi\phi} = C_L^{\phi\phi} \left(\frac{1}{\rho_L} - 1 \right), \tag{A8}$$

where

$$\rho_L = \frac{\langle \phi_{\mathrm{LM}}^{\mathrm{true}} \bar{\phi}_{\mathrm{LM}} \rangle}{\sqrt{\langle \phi_{\mathrm{LM}}^{\mathrm{true}} \phi_{\mathrm{LM}}^{\mathrm{true}} \rangle \langle \bar{\phi}_{\mathrm{LM}} \bar{\phi}_{\mathrm{LM}} \rangle}} \tag{A9}$$

is the average correlation coefficient between the true and estimated lensing potential. This allows computing the effective noise without ever explicitly debiasing the lensing estimate to remove the bias, A.

The per-mode noise enters the error bars on the estimated lensing power spectrum as

$$\langle (\Delta C_L^{\phi\phi})^2 \rangle = \frac{2(C_L^{\phi\phi} + N_L^{\phi\phi})^2}{(f_{\mathrm{sky}}(2L+1))}. \tag{A10}$$

Our MUSE forecasts do not compute an unbiased lensing map estimate, $\hat{\phi}_{\mathrm{LM}}$, nor do they explicitly compute $N_L^{\phi\phi}$ or use Equation (A10). Instead, MUSE directly computes the total posterior band power covariance, including signal and noise contributions, using Equation (A6). It is useful, however, to explore the effective noise levels that are reached. This can be conveniently performed by computing the averages in ρ_L via Monte Carlo methods, where the biased lensing map estimate, $\bar{\phi}$, is the MAP estimate of ϕ, which is a byproduct of the MUSE inference procedure.

Appendix B
Additional Details about Parameter Constraints

In Table 5 we present the constraints on the single-parameter extensions to ΛCDM from all the SPT-3G data sets. A comparison of the Ext-10k data set with Planck is presented in Figure 9. In Table 6, we present the degradation in cosmological parameters when we add one more parameter to the ΛCDM model. This is the same as the information presented in Figure 10.

Table 5
Forecasted 1σ Errors on Single-parameter Extensions to the ΛCDM for Various SPT-3G Surveys in Combination with Planck

Parameter		SPT-3G Main	SPT-3G Summer	SPT-3G Wide	Ext-4k	Ext-10k
N_{eff}	$[10^{-2}]$	10.1	10.9	9.23	8.27	6.75
n_{run}	$[10^{-3}]$	4.94	4.99	4.59	4.44	3.93
Ω_k	$[10^{-3}]$	2.46	2.49	2.38	2.35	2.26
$\sum m_\nu[\mathrm{eV}]$	$[10^{-2}]$	5.99	6.15	5.91	5.78	5.57
w_0	$[10^{-2}]$	10.23	10.44	10.03	9.91	9.64
Y_P	$[10^{-3}]$	6.48	6.68	5.75	5.34	4.43
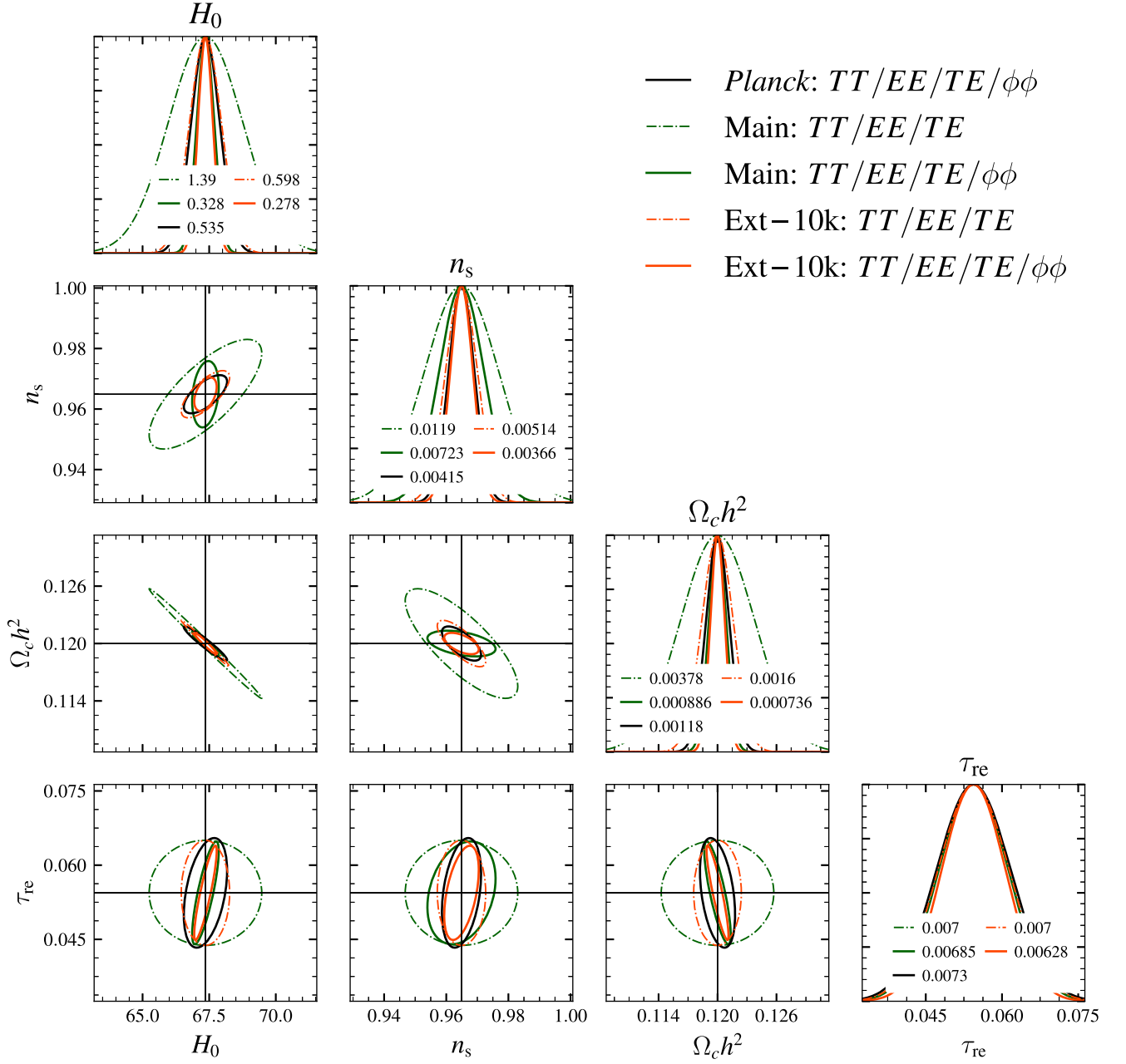
Figure 13. Marginalized one-dimensional and two-dimensional 68% contours for Hubble constant(H_0), scalar spectral index (n_s), cold dark matter density ($\Omega_c h^2$), and optical depth (τ_{re}), using the MUSE method, for SPT-3G Main (dark green), Ext-10k (orange), and Planck (black). The dashed–dotted curves show the constraints from delensed $TT/TE/EE$ spectra, whereas the solid curves also include lensing power spectrum information. The inclusion of the lensing spectrum significantly helps to break the degeneracies, especially for the SPT-3G Main survey. The 1σ errors are listed in the legend.
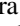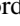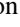
Table 6
Degradation in Constraints on Standard Cosmological Parameters When the ΛCDM Model is Extended by Single Additional Parameters

Parameter	$A_s[10^{-11}]$	$H_0\ [10^{-1}]$	$n_s\ [10^{-3}]$	$\Omega_b h^2[10^{-5}]$	$\Omega_c h^2[10^{-4}]$	$\tau_{re}[10^{-3}]$
ΛCDM	2.29	2.78	2.83	5.67	7.10	6.19
N_{eff}	2.51	6.18	4.88	9.61	10.80	6.39
$n_{\text{run}} \equiv dn_s/d\ln k$	2.43	2.83	2.94	6.90	7.14	6.35
Ω_k	2.55	8.73	3.10	5.73	9.56	6.42
$\sum m_\nu[\text{eV}]$	2.78	7.84	3.00	5.77	9.19	6.90
w_0	2.75	28.35	2.72	5.62	6.53	7.02
Y_P	2.52	3.31	4.44	9.34	7.49	6.67

Note. Note that H_0 is poorly constrained when w_0 is allowed to vary.

19

In Figure 13, we demonstrate the parameter constraints from Planck in black, and SPT-3G Main in green and Ext-10k in orange using the MUSE method. For SPT-3G, we show the constraints that we get from delensed $TT/EE/TE$ CMB-only as the dashed–dotted curves and the ones with the inclusion of lensing $\phi\phi$ as the solid curves. It is evident from the figure that the inclusion of lensing, breaks parameter degeneracies, which helps in improving the constraints on many cosmological parameters.

ORCID iDs

K. Prabhu ⓘ https://orcid.org/0009-0001-4135-8645
S. Raghunathan ⓘ https://orcid.org/0000-0003-1405-378X
M. Millea ⓘ https://orcid.org/0000-0001-7317-0551
A. J. Anderson ⓘ https://orcid.org/0000-0002-4435-4623
M. Archipley ⓘ https://orcid.org/0000-0002-0517-9842
L. Balkenhol ⓘ https://orcid.org/0000-0001-6899-1873
A. N. Bender ⓘ https://orcid.org/0000-0001-5868-0748
B. A. Benson ⓘ https://orcid.org/0000-0002-5108-6823
F. Bianchini ⓘ https://orcid.org/0000-0003-4847-3483
L. E. Bleem ⓘ https://orcid.org/0000-0001-7665-5079
F. R. Bouchet ⓘ https://orcid.org/0000-0002-8051-2924
T. W. Cecil ⓘ https://orcid.org/0000-0002-7019-5056
P. M. Chichura ⓘ https://orcid.org/0000-0002-5397-9035
T. M. Crawford ⓘ https://orcid.org/0000-0001-9000-5013
C. Daley ⓘ https://orcid.org/0000-0002-3760-2086
D. Dutcher ⓘ https://orcid.org/0000-0002-9962-2058
K. R. Ferguson ⓘ https://orcid.org/0000-0002-4928-8813
A. Foster ⓘ https://orcid.org/0000-0002-7145-1824
R. Gualtieri ⓘ https://orcid.org/0000-0003-4245-2315
G. P. Holder ⓘ https://orcid.org/0000-0002-0463-6394
G. I. Noble ⓘ https://orcid.org/0000-0002-5254-243X
Z. Pan ⓘ https://orcid.org/0000-0002-6164-9861
K. A. Phadke ⓘ https://orcid.org/0000-0001-7946-557X
A. Rahlin ⓘ https://orcid.org/0000-0003-3953-1776
C. L. Reichardt ⓘ https://orcid.org/0000-0003-2226-9169
J. A. Sobrin ⓘ https://orcid.org/0000-0001-6155-5315
C. Umilta ⓘ https://orcid.org/0000-0002-6805-6188
N. Whitehorn ⓘ https://orcid.org/0000-0002-3157-0407
W. L. K. Wu ⓘ https://orcid.org/0000-0001-5411-6920

References

Abazajian, K., Addison, G. E., Adshead, P., et al. 2022, ApJ, 926, 54
Abbott, T. M. C., Aguena, M., Alarcon, A., et al. 2022, PhRvD, 105, 023520
Ade, P. A. R., Aghanim, N., Arnaud, M., et al. 2015, A&A, 580, A22
Ade, P. A. R., Ahmed, Z., Amiri, M., et al. 2021, PhRvL, 127, 151301
Aiola, S., Calabrese, E., Maurin, L., et al. 2020, JCAP, 2020, 047
Alam, S., Aubert, M., Avila, S., et al. 2021, PhRvD, 103, 083533
Aloni, D., Berlin, A., Joseph, M., Schmaltz, M., & Weiner, N. 2022, PhRvD, 105, 123516
Anderson, A. J., Ade, P. A. R., Ahmed, Z., et al. 2018, JLTP, 193, 1057
Asgari, M., Lin, C.-A., Joachimi, B., et al. 2021, A&A, 645, A104
Balkenhol, L., Dutcher, D., Ade, P. A. R., et al. 2021, PhRvD, 104, 083509
Bender, A. N., Ade, P. A. R., Ahmed, Z., et al. 2018, Proc. SPIE, 10708, 1070803
Benson, B. A., Ade, P. A. R., Ahmed, Z., et al. 2014, Proc. SPIE, 9153, 91531P
Bianchini, F., Wu, W. L. K., Ade, P. A. R, et al. 2020, ApJ, 888, 119
Bleem, L. E., Stalder, B., de Haan, T., et al. 2015, ApJS, 216, 27
Bleem, L. E., Bocquet, S., Stalder, B., et al. 2020, ApJS, 247, 25
Bleem, L. E., Klein, M., Abbott, T. M. C., et al. 2024, OJAp, 7, 13
Bocquet, S., Grandis, S., Bleem, L. E., et al. 2024, arXiv:2401.02075

Cardoso, J.-F., Le Jeune, M., Delabrouille, J., Betoule, M., & Patanchon, G. 2008, ISTSP, 2, 735
Chiang, C.-T., & Slosar, A. 2018, arXiv:1811.03624
Chichura, P. M., Foster, A., Patel, C., et al. 2022, ApJ, 936, 173
Choi, S. K., Hasselfield, M., Ho, S.-P. P., et al. 2020, JCAP, 2020, 045
Copi, C. J., Huterer, D., Schwarz, D. J., & Starkman, G. D. 2010, AdAst, 2010, 847541
Cyburt, R. H., Fields, B. D., Olive, K. A., & Yeh, T.-H. 2016, RvMP, 88, 015004
Cyr-Racine, F.-Y., Ge, F., & Knox, L. 2022, PhRvL, 128, 201301
Dark Energy Survey and Kilo-Degree Survey Collaboration 2023, OJAp, 6, 36
Datta, R., Aiola, S., Choi, S. K., et al. 2019, MNRAS, 486, 5239
DES Collaboration 2024, arXiv:2401.02929
Dutcher, D., Balkenhol, L., Ade, P. A. R., et al. 2021, PhRvD, 104, 022003
Dutcher, D., Balkenhol, L., Ade, P. A. R., et al. 2021, PhRvD, 104, 022003
Everett, W. B., Zhang, L., Crawford, T. M., et al. 2020, ApJ, 900, 55
Finkbeiner, D. P., Galli, S., Lin, T., & Slatyer, T. R. 2012, PhRvD, 85, 043522
Galli, S., Pogosian, L., Jedamzik, K., & Balkenhol, L. 2022, PhRvD, 105, 023513
Galli, S., Slatyer, T. R., Valdes, M., & Iocco, F. 2013, PhRvD, 88, 063502
Galli, S., Wu, W. L. K., Benabed, K., et al. 2021, PhRvD, 104, 023518
Galli, S., Benabed, K., Bouchet, F., et al. 2014, PhRvD, 90, 063504
Givans, J. J., & Kamionkowski, M. 2023, arXiv:2311.06196
Guns, S., Foster, A., Daley, C., et al. 2021, ApJ, 916, 98
Gupta, N., Reichardt, C. L., Ade, P. A. R., et al. 2019, MNRAS, 490, 5712
Hart, L., & Chluba, J. 2018, MNRAS, 474, 1850
Hart, L., & Chluba, J. 2020a, MNRAS, 493, 3255
Hart, L., & Chluba, J. 2020b, MNRAS, 495, 4210
Heymans, C., Tröster, T., Asgari, M., et al. 2020, A&A, 646, A140
Hirata, C. M., & Seljak, U. 2003a, PhRvD, 67, 043001
Hirata, C. M., & Seljak, U. 2003b, PhRvD, 68, 083002
Hood, J. C. I., Simpson, A., McDaniel, A., et al. 2023, ApJL, 945, L23
Hotinli, S. C., Meyers, J., Trendafilova, C., Green, D., & van Engelen, A. 2022, JCAP, 2022, 020
Hou, Z., Aylor, K., Benson, B. A., et al. 2018, ApJ, 853, 3
Hu, W. 1998, ApJ, 506, 485
Hu, W., & Okamoto, T. 2002, ApJ, 574, 566
Huang, N., Bleem, L. E., Stalder, B., et al. 2020, AJ, 159, 110
Hughes, E., Ge, F., Cyr-Racine, F.-Y., Knox, L., & Raghunathan, S. 2024, PhRvD, 109, 103516
Jedamzik, K., & Pogosian, L. 2020, PhRvL, 125, 181302
Joudaki, S., Hildebrandt, H., Traykova, D., et al. 2020, A&A, 638, L1
Jungman, G., Kamionkowski, M., Kosowsky, A., & Spergel, D. N. 1996, PhRvL, 76, 1007
Khalife, A., Bahrami Zanjani, M., Galli, S., et al. 2024, JCAP, 2024, 059
Knox, L. 1995, PhRvD, 52, 4307
Knox, L., & Millea, M. 2020, PhRvD, 101, 043533
Kuijken, K., Heymans, C., Dvornik, A., et al. 2019, A&A, 625, A2
Lee, N., Ali-Haïmoud, Y., Schöneberg, N., & Poulin, V. 2023, PhRvL, 130, 161003
Lewis, A., Challinor, A., & Lasenby, A. 2000, ApJ, 538, 473
Louis, T., Addison, G. E., Hasselfield, M., et al. 2014, JCAP, 7, 016
Lynch, G. P., Knox, L., & Chluba, J. 2024, arXiv:2404.05715
Madhavacheril, M. S., Smith, K. M., Sherwin, B. D., & Naess, S. 2020, JCAP, 2021, 028
Madhavacheril, M. S., Qu, F. J., Sherwin, B. D., et al. 2024, ApJ, 962, 113
Meiers, M., Knox, L., & Schöneberg, N. 2023, PhRvD, 108, 103527
Millea, M., Anderes, E., & Wandelt, B. D. 2019, PhRvD, 100, 023509
Millea, M., Knox, L., & Fields, B. D. 2015, PhRvD, 92, 023010
Millea, M., & Seljak, U. 2022, PhRvD, 105, 103531
Millea, M., Daley, C. M., Chou, T. L., et al. 2021, ApJ, 922, 259
Murakami, Y. S., Riess, A. G., Stahl, B. E., et al. 2023, JCAP, 2023, 046
Pan, Z., Bianchini, F., Wu, W. L. K., et al. 2023, PhRvD, 108, 122005
Particle Data Group, Zyla, P. A., Barnett, R. M., et al. 2020, PTEP, 2020, 083C01
Peloton, J., Schmittfull, M., Lewis, A., Carron, J., & Zahn, O. 2017, PhRvD, 95, 043508
Planck Collaboration, Ade, P. A. R., Aghanim, N., et al. 2014, A&A, 571, A12
Planck Collaboration, Adam, R., Ade, P. A. R., et al. 2016a, A&A, 594, A9
Planck Collaboration, Ade, P. A. R., Aghanim, N., et al. 2016b, A&A, 594, A13
Planck Collaboration, Aghanim, N., Akrami, Y., et al. 2020, A&A, 641, A6
Qu, F. J., Sherwin, B. D., Madhavacheril, M. S., et al. 2024, ApJ, 962, 112
Raghunathan, S. 2022, ApJ, 928, 16

Raghunathan, S., & Omori, Y. 2023, ApJ, 954, 83
Raghunathan, S., Ade, P. A. R., Anderson, A. J., et al. 2024, arXiv:2403.02337
Rashkovetskyi, M., Muñoz, J. B., Eisenstein, D. J., & Dvorkin, C. 2021, PhRvD, 104, 103517
Reichardt, C. L., Patil, S., Ade, P. A. R., et al. 2021, ApJ, 908, 199
Riess, A. G., Yuan, W., Macri, L. M., et al. 2022, ApJL, 934, L7
Schiappucci, E., Bianchini, F., Aguena, M., et al. 2023, PhRvD, 107, 042004
Schöneberg, N., Abellán, G. F., Sánchez, A. P., et al. 2022, PhR, 984, 1
Sekiguchi, T., & Takahashi, T. 2021, PhRvD, 103, 083507
Sekiguchi, T., & Takahashi, T. 2021, PhRvD, 103, 083507
Simard, G., Omori, Y., Aylor, K., et al. 2018, ApJ, 860, 137
Simons Observatory Collaboration 2019, JCAP, 2019, 056

Slatyer, T. R., & Wu, C.-L. 2017, PhRvD, 95, 023010
Sobrin, J. A., Ade, P. A. R., Ahmed, Z., et al. 2018, Proc. SPIE, 10708, 107081H
Sobrin, J. A., Anderson, A. J., Bender, A. N., et al. 2022, ApJS, 258, 42
Tandoi, C., Guns, S., Foster, A., et al. 2024, ApJ, 972, 6
Tegmark, M., Taylor, A. N., & Heavens, A. F. 1997, ApJ, 480, 22
Thorne, B., Dunkley, J., Alonso, D., & Næss, S. 2017, MNRAS, 469, 2821
Trendafilova, C. 2023, JCAP, 2023, 071
Tristram, M., Banday, A. J., Douspis, M., et al. 2024, A&A, 682, A37
Whitehorn, N., Natoli, T., Ade, P. A. R., et al. 2016, ApJ, 830, 143
Zaldarriaga, M., Spergel, D. N., & Seljak, U. 1997, ApJ, 488, 1